

# Chemical evolution in the early phases of massive star formation II: Deuteration

T. Gerner<sup>1</sup>, Y. L. Shirley<sup>2</sup>, H. Beuther<sup>1</sup>, D. Semenov<sup>1</sup>, H. Linz<sup>1</sup>, T. Albertsson<sup>1</sup>, and Th. Henning<sup>1</sup>

<sup>1</sup> Max-Planck-Institut für Astronomie, Königstuhl 17, D-69117 Heidelberg, Germany

<sup>2</sup> Steward Observatory, University of Arizona, Tucson, AZ 85721, USA  
e-mail: gerner@mpia.de

October 13, 2018

## ABSTRACT

The chemical evolution in high-mass star-forming regions is still poorly constrained. Studying the evolution of deuterated molecules allows to differentiate between subsequent stages of high-mass star formation regions due to the strong temperature dependence of deuterium isotopic fractionation. We observed a sample of 59 sources including 19 infrared dark clouds, 20 high-mass protostellar objects, 11 hot molecular cores and 9 ultra-compact HII regions in the (3-2) transitions of the four deuterated molecules, DCN, DNC, DCO<sup>+</sup> and N<sub>2</sub>D<sup>+</sup> as well as their non-deuterated counterpart.

The overall detection fraction of DCN, DNC and DCO<sup>+</sup> is high and exceeds 50% for most of the stages. N<sub>2</sub>D<sup>+</sup> was only detected in a few infrared dark clouds and high-mass protostellar objects. It can be related to problems in the bandpass at the frequency of the transition and to low abundances in the more evolved, warmer stages. We find median D/H ratios of 0.02 for DCN, 0.005 for DNC, 0.0025 for DCO<sup>+</sup> and 0.02 for N<sub>2</sub>D<sup>+</sup>. While the D/H ratios of DNC, DCO<sup>+</sup> and N<sub>2</sub>D<sup>+</sup> decrease with time, DCN/HCN peaks at the hot molecular core stage. We only found weak correlations of the D/H ratios for N<sub>2</sub>D<sup>+</sup> with the luminosity of the central source and the FWHM of the line, and no correlation with the H<sub>2</sub> column density. In combination with a previously observed set of 14 other molecules (Paper I) we fitted the calculated column densities with an elaborate 1D physico-chemical model with time-dependent D-chemistry including ortho- and para-H<sub>2</sub> states. Good overall fits to the observed data have been obtained the model. It is one of the first times that observations and modeling have been combined to derive chemically based best-fit models for the evolution of high-mass star formation including deuteration.

**Key words.** Stars: formation – Stars: early-type – ISM: molecules – (ISM:) evolution – Astrochemistry

## 1. Introduction

The chemical evolution in high-mass star formation is still poorly understood and a field of intense investigations. The question of which molecules are to be used to distinguish between different evolutionary stages is of great interest. Those so called chemical clocks could be used to derive lifetimes of the different stages and help to infer the absolute ages of those objects. In addition, studying deuterium chemistry is also very useful to constrain physical parameters as for example the ionization fraction, temperature and density (e.g., Crapsi et al. 2005; Chen et al. 2011). In particular, deuterated molecules are very prominent candidates for probing this evolutionary sequence, since their chemistry depends highly on the temperature and the thermal history of an object (Caselli & Ceccarelli 2012; Albertsson et al. 2013). The deuteration fraction (the ratio between the column density of a deuterated molecule and its non-deuterated counterpart) is therefore an important parameter in order to study these evolutionary effects.

Theoretical and observational deuteration studies of low-mass star-forming regions revealed a large increase by several orders of magnitude in the deuteration fraction of starless cores with respect to the cosmic atomic D/H ratio of  $\sim 10^{-5}$  (Linsky 2003; Oliveira et al. 2003) and discussed possible trends with the evolutionary state of the star-forming region (e.g., Caselli et al. 2002; Crapsi et al. 2005; Bourke et al. 2012; Friesen et al. 2013). Correlations of the deuteration fraction were seen, e.g., with the

dust temperature and the level of CO depletion (Emprechtinger et al. 2009) or with the density (Daniel et al. 2007). Whether the deuterium chemistry during high-mass star formation behaves similar to that of low-mass cores is poorly constrained by observations so far. The current studies mostly target single deuterated species instead of a larger set of molecules, or are focused on a limited number of sources. Miettinen et al. (2011) found deuteration fractions in a sample of seven massive clumps associated with IRDCs that are lower than the values found in low-mass starless cores. Early studies of very young IRDCs by Pillai et al. (2007) and more evolved HMPOs by Fontani et al. (2006) indicated a trend of higher deuteration fractions for the younger, cooler sources. A recent attempt to systematically study a larger sample of different evolutionary stages by Fontani et al. (2011) revealed that the N<sub>2</sub>D<sup>+</sup>/N<sub>2</sub>H<sup>+</sup> column density ratio is an indicator for the evolutionary stage in high-mass star formation. Chen et al. (2011) observed several dense cores covering different evolutionary stages in three massive star-forming clouds and studied the deuteration fraction of N<sub>2</sub>H<sup>+</sup> and the role of CO depletion in this context. They found a clear trend of decreasing deuteration fraction with increasing gas temperature tracing different evolutionary stages. They also found an increasing trend of the deuteration fraction with the CO depletion factor, which is similarly seen in low-mass protostellar cores.

In order to study the deuteration in high-mass star-forming regions in an evolutionary sense, we divide the high-mass star formation sequence into different stages (see also Gerner

arXiv:1503.06594v1 [astro-ph.GA] 23 Mar 2015

et al. 2014). Beuther et al. (2007a); Zinnecker & Yorke (2007); Tan et al. (2014) divided the evolutionary sequence into different phases based on their physical conditions. We describe the evolutionary picture from an observationally point of view and distinguish between 4 observationally motivated stages based on the underlying physical sequence. First, our picture starts with an initially starless infrared dark cloud phase (IRDC). At this point these objects are close to isothermal and consist of cold and dense gas and dust. In this approach we do not consider a long living pre-IRDC phase, which is proposed in theoretical works (e.g., Narayanan et al. 2008; Heitsch et al. 2008) and also supported by observations (e.g., Barnes et al. 2011). This phase should be less dense and in our model we define the year zero of our evolutionary sequence when the densities start to be higher than  $10^4 \text{ cm}^{-3}$ . While starless IRDCs only emit in the (sub-)millimeter regime, places of beginning star-formation start to show up as point sources at  $\mu\text{m}$ -wavelengths. Eventually, the overdensities within the IRDC begin to collapse and form one or several accreting protostars with  $> 8 M_{\odot}$  in the next phase, that is a high-mass protostellar object (HMPO). The internal sources of HMPOs emit at mid-infrared wavelengths and their radiation starts to heat up the environment, leading to non-isothermal temperature profiles. The higher temperatures boost the molecular complexity leading to the hot molecular core phase (HMC). This phase is from a physical point a sub-group of the HMPO phase, but clearly distinguishes from a chemical point of view, driven by the higher temperatures that liberate molecules from molecular-rich ices and increase the molecular complexity of the source. Finally, the UV-radiation of the central star(s) ionizes the ambient gas and create an ultra-compact HII region (UCHII). That is the last stage considered in our evolutionary picture. These objects presumably have stopped accreting and complex molecules seen in the HMC phase are not longer detectable. It is possible that overlaps occur between these stages, leading to HMCs associated with UCHII regions and even still accreting protostars within UCHII regions. High-mass star-forming sites are complex objects. In order to circumvent the problem of the coexistence of different stages in one object, we want to statistically characterize the evolution along the different stages.

In this work we continue and extend an investigation of the chemical evolution in 59 high-mass star forming regions in different evolutionary stages (Gerner et al. 2014) towards deuterated molecules. In the previous work we measured the beam averaged column densities of 14 different molecular species and derived a chemical evolutionary picture across the evolutionary sequence in high-mass star formation starting with IRDCs via HMPOs to HMCs and finally UCHII regions. We found that overall the chemical complexity, column densities and abundances increase with evolutionary stage. We fitted the data with a 1D physico-chemical modeling approach and found good agreement with the observations. Here we want to measure the deuteration fractions of the four deuterated molecules DCN, DNC, DCO<sup>+</sup> and N<sub>2</sub>D<sup>+</sup> and test their correlations with evolutionary stage and with physical parameters such as the luminosity of the objects. Furthermore, we model the derived column densities with a state-of-the-art 1D deuterium chemical model along the evolutionary sequence from IRDCs via HMPOs to HMCs and UCHII regions.

The structure of the paper is the following. In Section 2 we introduce the source sample, followed by a description of the observations in Section 3 and an introduction to deuterium fractionation in Section 4. In Section 5 we present the results of the analyzed observational data. In Section 6 we introduce the model

used to fit the data and discuss the modeling results as well as their implications. We conclude with a summary in Section 7.

## 2. Source sample

The sources are taken from Gerner et al. (2014) and initially selected from different source lists. The total sample contains 59 high-mass star-forming regions, consisting of 19 IRDCs and 20 HMPOs as well as 11 HMCs and 9 UCHII. The sources were selected from well known source catalogs of the literature without specific selection criteria such as spherical symmetry. The lists of the IRDCs were first presented in Carey et al. (2000) and Sridharan et al. (2005) and are part of the *Herschel* guaranteed time key project EPOS (The Early Phase of Star Formation, Ragan et al. 2012). This sample consists of 6 IRDCs showing no internal point sources below  $70\mu\text{m}$  and 13 IRDCs that have internal point sources at  $24\mu\text{m}$  and  $70\mu\text{m}$ . The HMPOs are taken from the well-studied sample by Sridharan et al. (2002) and Beuther et al. (2002b,c). HMC sources are selected from the line-rich sample of Hatchell et al. (1998), including a few additional well-known HMCs: W3IRS5, W3H<sub>2</sub>O and Orion-KL. For the UCHII regions, we selected line-poor high-mass star-forming regions from Hatchell et al. (1998), and additional sources from Wood & Churchwell (1989b). Recent studies towards single sources of the ones included in this work overall confirm the evolutionary classification given in the referenced papers. The full source list is given in Table A.1. The table gives also the distance of each source. In the cases that the distance ambiguity of near and far kinematic solution could not be resolved we used the near kinematic solution. In Figure 1 we show the distribution of the distances for all four subsamples including their median and mean value. The median and mean distance for the IRDCs, HMPOs and HMCs are very similar with values around 4kpc. Thus, the larger range of distances of the total sample should not affect the comparison between the median or mean properties of the different subsamples, e.g., their detection statistics or their derived median column densities (e.g., due to uncertain beam filling fractions). Only the UCHII subsample shows significantly larger distances. However, since this subsample is not of our main interest in this work, this does not dramatically influence the results of this study.

## 3. Observations

The 59 sources were observed with the Arizona Radio Observatory Submillimeter Telescope (SMT) in 2013 between February 12-15, March 10-13 and on March 31 and April 1 with  $\sim 100$  h total observing time. For the observations we used the ALMA type 1.3 mm dual polarization sideband separating heterodyne receiver and the filterbanks as backends with a resolution of 250 kHz which corresponds to  $\sim 0.3 \text{ km s}^{-1}$  resolution in velocity. The beam size of the SMT at 1.3 mm is  $\sim 30''$ . One single integration took 5 min in position-switching mode, with 2.5 minutes on-source time. The emission in the deuterated lines were integrated 2-3 times and the emission in the non-deuterated lines 1-2 times, depending on the observing conditions. The data was calibrated using data of Jupiter from the same observation runs assuming a sideband rejection of 13db. The mean system temperatures of the spectra  $T_{\text{sys}}$  is 380 K. The data reduction was conducted with the standard GILDAS<sup>1</sup> software package CLASS. All spectra from each source were baseline subtracted, calibrated to  $T_{\text{mb}}$  scale with typical beam efficiencies of 0.6 and

<sup>1</sup> <http://www.iram.fr/IRAMFR/GILDAS>

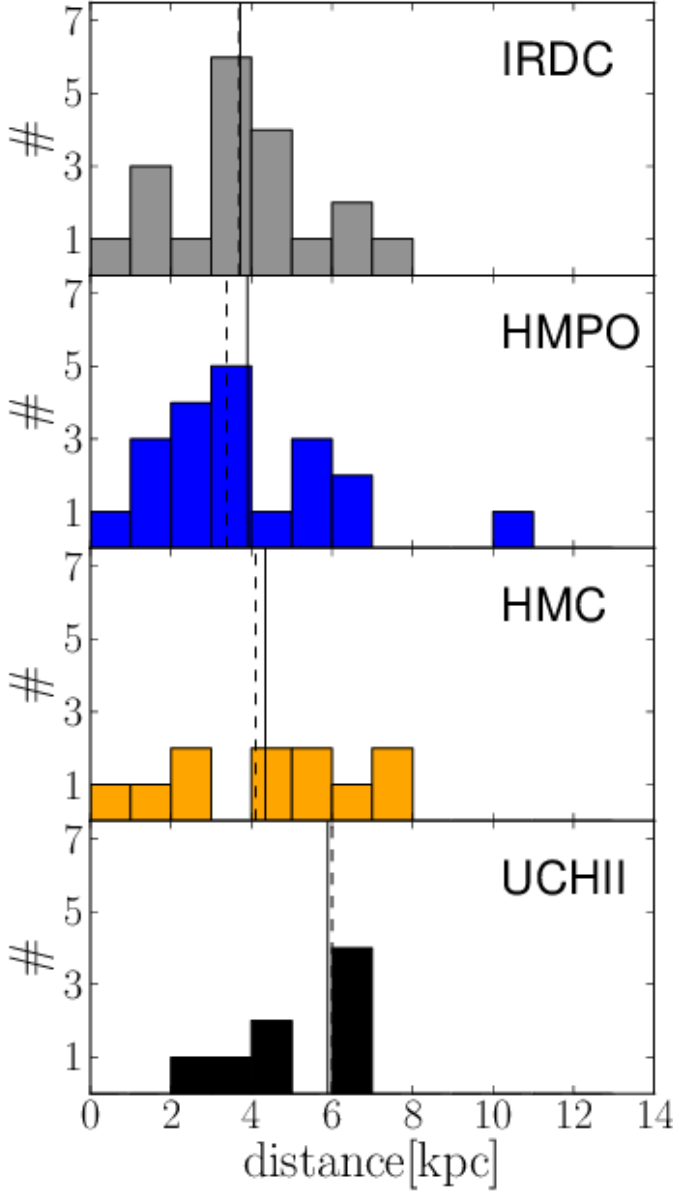


**Fig. 1.** From top to bottom: distance distribution for each of the subsamples, IRDCs, HMPOs, HMCs and UCHII regions. The bins have widths of 1 kpc and show the number of sources per distance range. The vertical dashed line shows the median distance and the vertical solid line the mean distance of the subsample.

averaged. In few cases we used the 1 MHz filterbanks spectra due to very broad lines (e.g., in Orion-KL) or when the line was not detected in the 250 kHz filterbanks (with 128 channels) but in the 1 MHz filterbanks (with 512 channels). The line integrals were measured by summing the line emission channel by channel for detected lines. The detection criteria is  $S/N > 3$ .

The line parameters of the observed molecules are given in Table 1.

### 3.1. RMS

The median  $1\sigma$  rms values for the deuterated molecules are 0.031 K for DCN (3-2), 0.024 K for DNC (3-2), 0.025 K for DCO<sup>+</sup> (3-2) and 0.035 K for N<sub>2</sub>D<sup>+</sup> (3-2). DCN (3-2) was ob-

**Table 1.** List of analyzed molecules with transitions, frequencies, energies of the upper level, and Einstein coefficients  $A_{ul}$ .

Molecule	Transition	Frequency [GHz]	$E_u/k$ [K]	$A_{ul}$ [ $10^{-3} \times s^{-1}$ ]
DCO <sup>+</sup>	3-2	216.1126	20.74	0.772
DCN	3-2	217.2385	20.85	0.457
DNC	3-2	228.9105	21.97	0.557
N <sub>2</sub> D <sup>+</sup>	3-2	231.3218	22.20	0.712
H <sup>13</sup> CO <sup>+</sup>	3-2	260.2553	24.98	1.337
HCN	3-2	265.8864	25.52	0.836
HCO <sup>+</sup>	3-2	267.5576	25.68	1.476
HNC	3-2	271.9811	26.11	0.934
N <sub>2</sub> H <sup>+</sup>	3-2	279.5117	26.82	1.259

**Notes.** Values are taken from LAMDA database (Schöier et al. 2005).

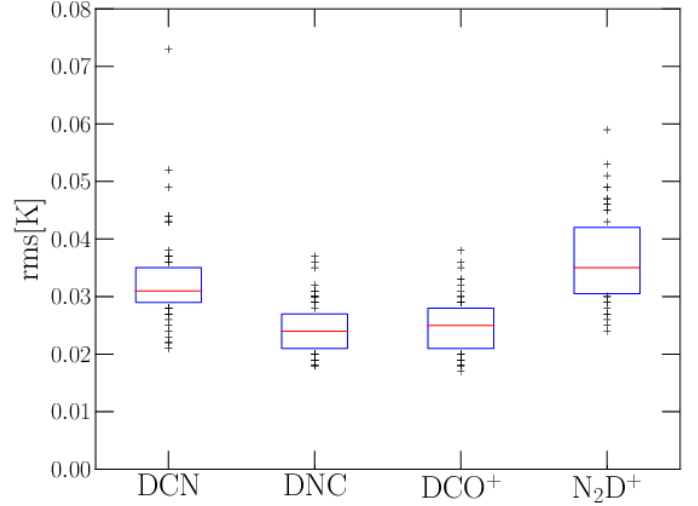


**Fig. 2.**  $1\sigma$  rms values of spectra of the deuterated molecules. The red solid line shows the median, the blue box the 25%-75% range and the crosses mark the outliers.

served in the later shifts and the higher rms value is due to worse observing conditions during that period. The higher rms value for N<sub>2</sub>D<sup>+</sup> (3-2) is due to problems at this specific transition frequency and described in the following Section. An overview of all rms values is given in Figure 2. The strong outlier in DCN (3-2) is from Orion-KL which is still a detection.

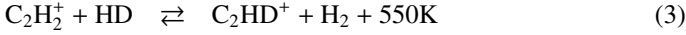
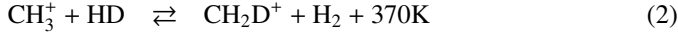
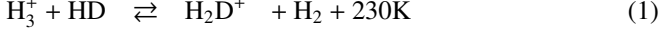
### 3.2. Problems with N<sub>2</sub>D<sup>+</sup> spectra

Reducing and analyzing the spectra of the N<sub>2</sub>D<sup>+</sup> (3-2) transition at 231.32 GHz was problematic due to blending by an overlaying pressure broadened ozone line in the atmosphere. This ozone line depends on the elevation of the source and time of the observation and affects the different sources with varying strength. Due to this contamination, the mean  $1\sigma$  rms value of the N<sub>2</sub>D<sup>+</sup> line is 40% higher than for the other deuterated spectral lines and thus the threshold for a detection is higher. In the 5 sources IRDC18454.1, IRDC18454.3, Orion-KL, HMC010.47 and HMC031.41 the ozone line makes it impossible to discriminate between a detection or a non-detection.

## 4. Deuterium fractionation

Under cold conditions, the deuteration fraction of molecules can be enhanced through reactions with, e.g., deuterated H<sub>3</sub><sup>+</sup>, H<sub>2</sub>D<sup>+</sup>. While the chemical reaction that deuterates H<sub>3</sub><sup>+</sup> proceeds without

a thermal barrier, the backward reaction is endothermic and has a thermal energy barrier (Watson 1974; Caselli & Ceccarelli 2012; Albertsson et al. 2013). This energy barrier leads to an enhanced formation fraction at low temperatures, but becomes negligible for higher temperatures at which the backward reaction becomes as efficient as the forward reaction. The chemical reactions and their energy barriers that introduce deuterium into some of the key molecules are the following:



The temperature range for an effective D-enhancement for the pathway via  $\text{H}_3^+$  isotopologues is  $\sim 10 - 30$  K, whereas it is  $\sim 10 - 80$  K for pathways via light hydrocarbons (Millar et al. 1989; Albertsson et al. 2013). This enhances the deuteration fraction of the key molecules  $\text{H}_3^+$  and  $\text{CH}_3^+$  in different temperature regimes. Another effect that increases the  $\text{H}_2\text{D}^+/\text{H}_3^+$  ratio is the depletion of neutral gas-phase species (e.g., CO,  $\text{N}_2$ ) (see Dalgarno & Lepp 1984; Roberts & Millar 2000). This enhancement is then imprinted on the molecules formed through these reaction partners.

In the literature different models exist describing the formation routes of deuterated molecules and their relative importance. The dominant formation pathways of  $\text{DCO}^+$  and  $\text{N}_2\text{D}^+$  are via a low-temperature route through  $\text{H}_3^+$  isotopologues, whereas DCN can be formed via a fractionation route involving light hydrocarbons. The back-reaction of the route via  $\text{H}_3^+$  isotopologues sets in at temperatures around 30 K and their deuteration fractions decrease with rising temperature. According to Roueff et al. (2007), both DCN and DNC can be formed efficiently at low temperatures via deuteration of HNC or HCN. However, at higher temperatures DNC gets destroyed by reactions with atomic oxygen, unlike DCN. The chemical models of Turner (2001) indicate that only DCN is also formed via reactions with light hydrocarbons involved, but not DNC. If the Turner (2001) scheme is correct, then molecules such as  $\text{C}_2\text{D}$ , HD $\text{CO}$  or  $\text{C}_3\text{HD}$  should show a similar behavior like DCN with temperature, since they are also formed via  $\text{CH}_2\text{D}^+$  and  $\text{C}_2\text{HD}^+$ .

Parise et al. (2009) found a low  $\text{DCO}^+/\text{HCO}^+$  column density ratio but significant deuteration fractions for HCN and  $\text{H}_2\text{CO}$  under temperature conditions of  $\sim 70$  K towards the Orion Bar PDR. Model calculations by Roueff et al. (2007) predicted that in general the  $\text{DNC}/\text{HNC}$ ,  $\text{DCO}^+/\text{HCO}^+$  and  $\text{N}_2\text{D}^+/\text{N}_2\text{H}^+$  column density ratios decrease with temperature, but are almost constant with density. The  $\text{DCN}/\text{HCN}$  column density ratio shows a more complex behavior with temperature, reaching the largest ratio for  $\sim 30$  K, and shows a stronger increase with density. They found that the reason for this behavior is twofold. First, due to the enhanced abundance of radicals (e.g., CHD and  $\text{CD}_2$ ) that form DCN. Second, the main destruction pathways of DCN are reactions with the ions  $\text{HCO}^+$  and  $\text{H}_3\text{O}^+$ , that leads to  $\text{DCNH}^+$  which subsequently returns to DCN via dissociative recombination. The deuteration fractions also strongly depend on the assumed elemental abundances.

## 5. Results

### 5.1. Detection fractions for DCN, DNC, $\text{DCO}^+$ and $\text{N}_2\text{D}^+$

The detection fractions of DCN, DNC,  $\text{DCO}^+$  and  $\text{N}_2\text{D}^+$  in the single stages are shown in Figure 3. In this figure, the IRDC stage is split into the two categories of sources mentioned in Sect. 2,

without and with an embedded point source. From that figure we identify three trends:

1)  $\text{N}_2\text{D}^+(3-2)$  is only detected towards IRDCs and HMPOs. Since the  $\text{N}_2\text{H}^+$  abundance is almost constant over the full evolutionary sequence (Paper I), most likely a strong temperature dependence of the  $\text{N}_2\text{D}^+$  production leading to its disappearance at  $T \gtrsim 30$  K is the answer to its apparent absence in the HMC and UCH $\text{II}$  stages. Another complication is problems with the particular bandpass of its (3-2) transition mentioned in Sect. 3.2 which lead to a higher mean  $1\sigma$  rms value. That does not mean that  $\text{N}_2\text{D}^+$  is not present, since some of our sources with non-detections in  $\text{N}_2\text{D}^+(3-2)$  are detected by Fontani et al. (2011) in  $\text{N}_2\text{D}^+(2-1)$ . This could indicate the importance of excitation conditions for the detection of the (3-2) transitions. Nonetheless, the detection rates of  $\text{N}_2\text{D}^+(3-2)$  are clearly lower than the detection rates of the other observed molecular transitions of this work. 2) The only deuterated molecule detected in the presumably coldest IRDCs without an embedded point source at  $24\mu\text{m}$  (Spitzer/MIPSGAL) or  $70\mu\text{m}$  (Herschel/PACS) is  $\text{DCO}^+$  which has also the highest detection fraction in the more evolved IRDCs. 3) The detection fractions of DCN, DNC and  $\text{DCO}^+$  in warm IRDCs up to UCH $\text{II}$  regions are comparable and peak at the HMC stage. In general the detection fractions towards the observed high-mass star-forming regions are high,  $\gtrsim 60\%$ . It is important to mention here that the strength of a transition is the product of column density and temperature and thus detections at the lower temperatures present in the earlier stages are more difficult. A lower detection fraction does not necessarily mean that the column densities in the earlier stages are lower compared to the later stages. The differences in column densities along the evolutionary sequence is discussed in Sect 6.1.

### 5.2. Excitation temperatures and final column densities

In this section we discuss the excitation temperatures used to derive the column densities and how we combined the data from Paper I and this work to obtain the final column densities. The derivation of the column densities is shown in the appendix in Section A.1.

The column densities for the non-deuterated species were partly taken from Gerner et al. (2014) and partly calculated from the new observations. A detailed overview on the exact combination of the previous work and this one is given below. In the previous study we observed the (1-0)-transitions of several molecules with the IRAM 30m telescope. The size of the beam for those observed (1-0)-transitions is very close to the size of the beam of the (3-2)-transitions observed for this work with the SMT. In the previous work we used likely optically thin (1-0)-transitions of  $\text{H}^{13}\text{CO}^+$  and  $\text{HN}^{13}\text{C}$  and, due to their hyperfine structure, optical depth corrected  $\text{N}_2\text{H}^+$  and HCN to derive their column densities. The spectra of the first study were partly affected by source emission at the present off-positions and strong optical depth effects. In these cases the optical depth and the integrated intensity could not be reliably determined. Thus we refrained from using those lines in the analysis. In this work we have additional information from the (3-2) transitions to complement the missing column densities. In order to obtain consistent results from both observation runs we compared the column densities of  $\text{H}^{13}\text{CO}^+(1-0)$  with the column densities of  $\text{H}^{13}\text{CO}^+(3-2)$  derived with  $T_{\text{ex}} = 20.9$  K (IRDC),  $T_{\text{ex}} = 29.5$  K (HMPO),  $T_{\text{ex}} = 40.2$  K (HMC) and  $T_{\text{ex}} = 36.0$  K (UCH $\text{II}$ ). Those are the mean temperatures of the best-fit models from Gerner et al. (2014). The comparison is shown in Figure 4.

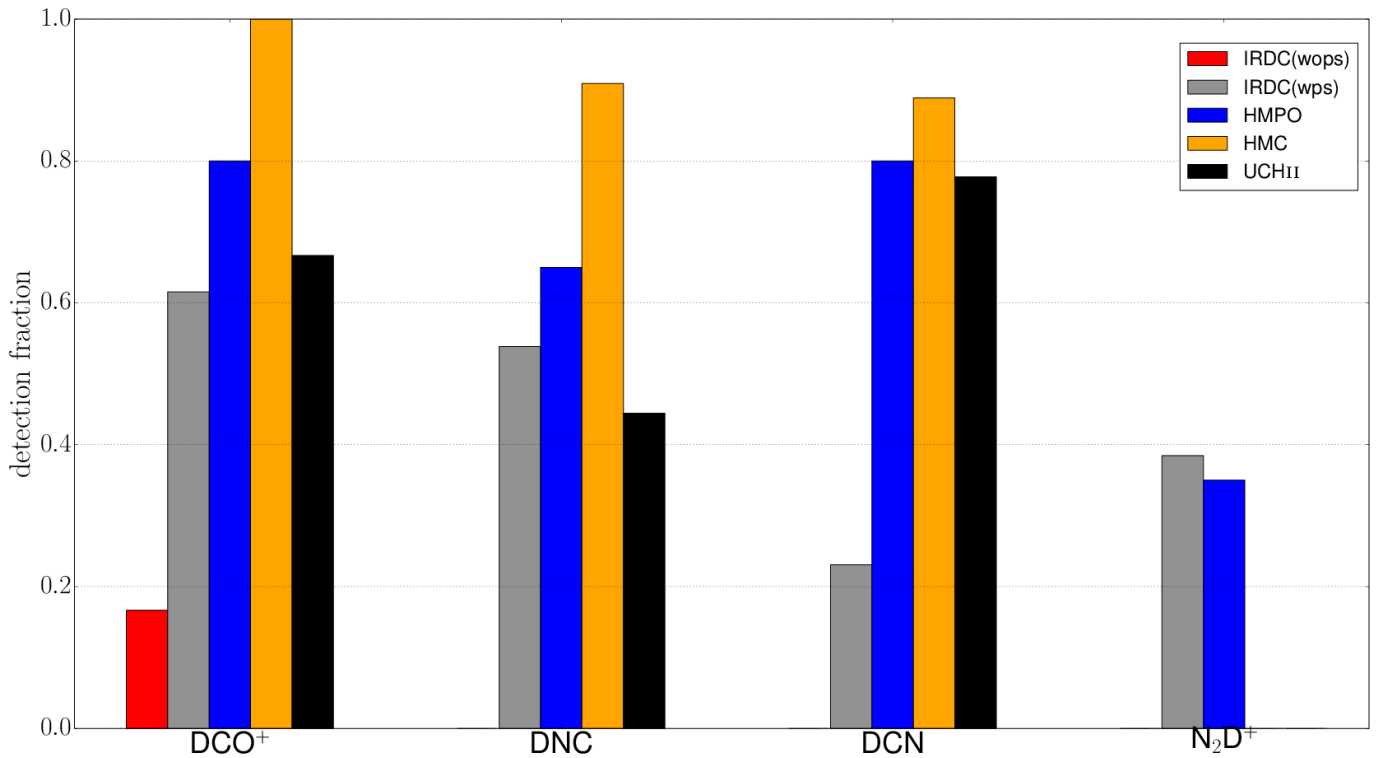


**Fig. 3.** Detection fraction of the 4 observed deuterated species in the different evolutionary stages. Here the infrared dark cloud (IRDC) stage is divided into the two subsamples without and with an embedded point source at 24 or 70  $\mu\text{m}$ , indicated in the caption as IRDC(wops) and IRDC(wps), respectively. The detection fractions are shown from left to right with infrared dark clouds without embedded point sources in red (IRDC(wops)), infrared dark clouds with embedded point sources (IRDC(wps)) in grey, high-mass protostellar objects (HMPO) in blue, hot molecular cores (HMC) in yellow and ultracompact HII regions (UCHII) in black.

The derived column densities for the IRAM data are clearly all higher. Excluding problems in the quality of the data and the calibration leads to the assumption that, while the (1-0) transitions are in LTE, the upper levels are sub-thermally populated and thus the (3-2) transitions are not in LTE. This implies that the average densities of the gas should be below  $\sim 10^6 - 10^7 \text{ cm}^{-3}$ . Since the two different lines trace gas with different excitation conditions, the spatial extent probed by both transitions might be different. However, we do not know the beam filling factors for the different molecules and their different transitions. In addition, we calculated the column densities from the  $\text{H}^{13}\text{CO}^+(1-0)$  and (3-2) transitions with the non-LTE radiative transfer code RADEX<sup>2</sup> (van der Tak et al. 2007). The derived column densities for  $\text{H}^{13}\text{CO}^+$  were within a factor of 2 in agreement with the column densities derived under the assumption of LTE from the  $\text{H}^{13}\text{CO}^+(1-0)$  transition. This is well within the uncertainties and validates the assumptions made for the (1-0) transitions. In order to compensate for the differences in the excitation conditions between (1-0) and (3-2) transitions, we calculated the excitation temperature of the (3-2) transition for each source which would be necessary to derive the total column densities derived from the (1-0) transition. From those excitation temperatures we computed the median value for each stage. That resulted in  $T_{\text{ex}} = 5.2$  (IRDC),  $T_{\text{ex}} = 6.2$  (HMPO),  $T_{\text{ex}} = 7.2$  (HMC) and  $T_{\text{ex}} = 6.4$  (UCH II) for the (3-2) transitions. The comparison of the calibrated  $\text{H}^{13}\text{CO}^+(3-2)$  column densities derived with the lower excitation temperatures and the (1-0) data is shown in Figure 4. This correction should also reduce the error in the beam filling fraction and make the different transitions comparable.

For the four different molecules we derived the column densities in the following way.

#### 5.2.1. $\text{HCO}^+$ and HNC

For  $\text{HCO}^+$  and HNC we used  $\text{H}^{13}\text{CO}^+(1-0)$  and  $\text{HN}^{13}\text{C}$  transitions, respectively, assuming the relative isotopic ratio depending on the galactocentric distance described in Wilson & Rood (1994). In Gerner et al. (2014) we used the representative value for the Sun and the local ISM of  $^{12}\text{C}/^{13}\text{C}=89$  (Lodders 2003). This lowers the derived column densities for this work.

#### 5.2.2. $\text{N}_2\text{H}^+$ and HCN

For  $\text{N}_2\text{H}^+$  we took the column densities from the (1-0) transitions from Gerner et al. (2014), for which we used, in case of optically thick lines, the optical depth and the excitation temperature from the hyperfine fits made with CLASS<sup>3</sup>. The hyperfine structure fitting routine (METHOD HFS) assumes that all components of the hyperfine structure have the same excitation temperature and the same width and that the components are separated in frequency by the laboratory values. From the comparison of the ratios of the line intensities of the hyperfine components to the theoretically expected ratios, the fit routine estimates the optical depth of the line. In the optically thick case that allows us to determine the excitation temperature. In the optically thin case we assumed the excitation temperatures given in Section 5.2.

<sup>2</sup> <https://www.sron.rug.nl/~vdtak/radex/index.shtml>

<sup>3</sup> <http://www.iram.fr/IRAMFR/GILDAS/doc/pdf/class.pdf>

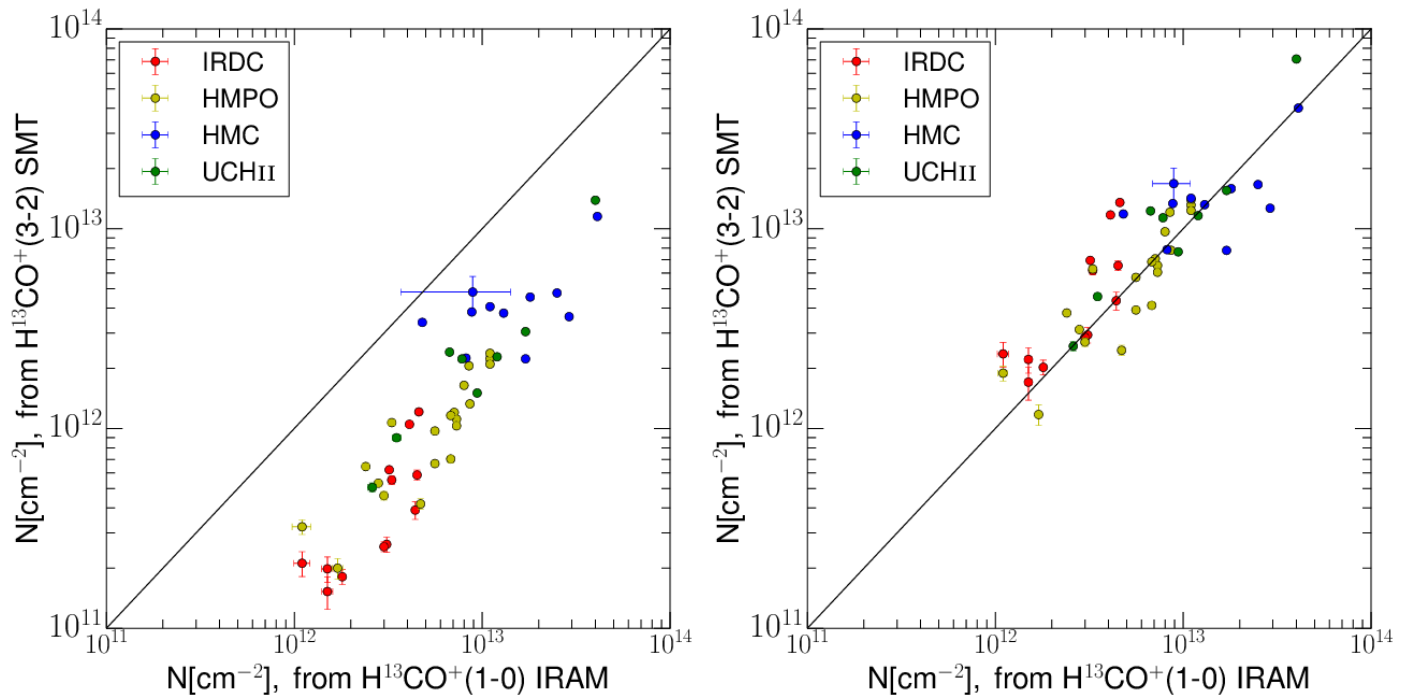


**Fig. 4.** Left: Comparison of column densities of  $\text{H}^{13}\text{CO}^+(1-0)$  and  $\text{H}^{13}\text{CO}^+(3-2)$  assuming the same excitation temperatures for both transitions. Right: Comparison of column densities of  $\text{H}^{13}\text{CO}^+(1-0)$  and  $\text{H}^{13}\text{CO}^+(3-2)$  using the excitation temperatures discussed in section 5.2. The errors show the uncertainties in the measured integrated flux. In some cases that uncertainty is too small to be seen on this plot.

For HCN we used the optical depth corrected column densities from the (1-0) transitions when available. In all other cases we computed the mean difference between column densities derived from the (1-0) transitions and the (3-2) transitions and applied this factor of  $\sim 1.7$  to the derived column densities from the (3-2) transitions.

All column densities are beam averaged quantities. The resulting median abundances including all detections and upper limits for each subsequent evolutionary phase are given in Tables 2. In the derivation of the column densities we assumed the excitation temperatures of the deuterated and non-deuterated molecule of the same transition to be equal. This assumption is valid for high densities and high excitation temperatures, but might lead to an underestimation of the deuteration column density ratios  $D_{\text{frac}}$  by a factor of  $\sim 2 - 4$  (Shirley 2015, in prep.).

## 6. Discussion

### 6.1. Deuteration fractions

The spread of the deuteration fractions  $D_{\text{frac}}$  as well as the median value for each stage is shown in Figure 5. These values include detections and upper limits. In the case of  $\text{N}_2\text{D}^+$  the median  $3\sigma$ -limits of non-detections for the HMC-stage and UCHII-stage are given, since the detection fraction is zero. These values can be considered as a sensitivity limit.

The ratios of the column densities of  $\text{DNC}$ ,  $\text{DCO}^+$  and  $\text{N}_2\text{D}^+$  with their non-deuterated counterparts  $\text{HNC}$ ,  $\text{HCO}^+$  and  $\text{N}_2\text{H}^+$  all show decreasing trends with evolutionary stage, despite the large spread of ratios within individual stages. Only HCN shows an increase in the ratio with the maximum reached in the HMC-stage. In some cases the consecutive stages appear not very different from each other within the error budget (e.g., HMPO-HMC of  $\text{DCO}^+/\text{HCO}^+$ , HMC-UCHII of  $\text{DNC}/\text{HNC}$ ). The likely reason for this is that the evolution along the sequence is con-

tinuous, and there might be overlaps between consecutive stages like, for example, some of the HMCs are associated with UCHII regions. One can distinguish between two different scenarios that can lead to an overlap between consecutive stages. In the cases like HMC029.96 (G29.96), high spatial resolution observations show a separation of the actual UCHII region and the neighboring HMC of  $2''$  (Cesaroni et al. 1994; Beuther et al. 2007b). The HMC and the UCHII region are two (or more) distinct entities. The second scenario is cases like HMC009.62 (G9.62), where also a separate UCHII region exists, but in addition a small hypercompact HII region is present at the location of the HMC itself (Testi et al. 2000). This is a general caveat in single-dish observations of HMCs that might be contaminated by UCHII regions in the beam. Here, the sources are classified based on their chemistry and that is likely dominated by the HMC. However, that does not totally cancel this effect and differences in the measured ratios between different stages are in some cases weaker. Nevertheless, the global trends are clearly visible.

Furthermore, Figure 6 shows the observed column density ratios of  $\text{DCN}/\text{DNC}$  and  $\text{HCN}/\text{HNC}$  for sources detected in both molecules, respectively. While the ratio of the non-deuterated molecules is almost constant, the ratio of the deuterated molecules shows clearly a peak at the HMC stage, reflected by the results of the one-way ANOVA tests that yield probability values  $p < 10^{-4}$  for  $\text{DCN}/\text{DNC}$  and  $p = 0.17$  in the case of  $\text{HCN}/\text{HNC}$ . The KS2 test of the consecutive stages confirms these findings. This leads to the conclusion that DCN can be formed more efficiently or is destroyed less efficiently than DNC in the more evolved and thus warmer sources. The observed behavior can be understood according to the dominant formation pathways scenario stated by Turner (2001). He claimed that all four deuterated molecules can be efficiently formed at low temperatures via  $\text{H}_2\text{D}^+$ , but only DCN can be formed at higher temperature via  $\text{CH}_2\text{D}^+$ . That would lead to the observed trends in the deuteration fractions, since DCN can still be formed in the

**Table 2.** Observed median column densities ( $N$ ) and the standard deviation ( $SD$ ) for IRDCs, HMPOs, HMCs and UCHII regions as  $a(x) = a \times 10^x$ . The median includes detections and upper limits of non-detections. Species detected in less than 50% of the sources are indicated by an upper limit.

	IRDC		HMPO		HMC		UCHII	
	$N$	$SD$	$N$	$SD$	$N$	$SD$	$N$	$SD$
	$\text{cm}^{-2}$	$\text{cm}^{-2}$	$\text{cm}^{-2}$	$\text{cm}^{-2}$	$\text{cm}^{-2}$	$\text{cm}^{-2}$	$\text{cm}^{-2}$	$\text{cm}^{-2}$
HCO <sup>+</sup>	7.9(13)	6.8(13)	3.7(14)	1.7(14)	7.6(14)	4.3(14)	3.8(14)	5.9(14)
HCN	7.2(13)	5.7(13)	1.3(14)	1.7(14)	3.5(14)	3.4(15)	3.4(14)	3.7(14)
HNC	9.7(13)	8.4(13)	2.9(14)	1.6(14)	5.5(14)	3.5(14)	2.0(14)	7.7(14)
N <sub>2</sub> H <sup>+</sup>	2.2(13)	1.5(13)	4.6(13)	3.2(13)	5.5(13)	4.6(13)	3.7(13)	6.4(13)
DCO <sup>+</sup>	≤3.1(11)	1.1(12)	6.7(11)	6.5(11)	2.0(12)	7.6(12)	4.6(11)	3.4(11)
DCN	≤6.1(11)	7.3(11)	2.0(12)	2.2(12)	8.0(12)	3.6(13)	1.9(12)	6.0(12)
DNC	≤6.1(11)	9.2(11)	1.0(12)	1.2(12)	8.7(11)	7.1(11)	≤3.0(11)	1.9(12)
N <sub>2</sub> D <sup>+</sup>	≤6.8(11)	4.3(11)	≤3.8(11)	4.0(11)	≤2.2(11)	6.6(10)	≤3.3(11)	4.6(10)

more evolved stages, in contrary to the other observed deuterated molecules. However, newer chemical models, e.g., from Roueff et al. (2007) or the updated model we use, do not support this scenario of a difference in dominant formation pathways between DCN and DNC. According to these new models, both isomers are formed from light hydrocarbons and thus exhibit a similar evolution in the abundance ratios with temperature. Hiraoka et al. (2006) were studying the association reactions of CN with D in laboratory experiments and found at a temperature of 10 K an intensity ratio of DNC/DCN of  $\sim 3$ . At temperatures  $> 20$  K, the formation of DNC and DCN became negligible. This is consistent with the derived value for the IRDC stage in this work on the order of unity, but contradicts the higher DCN/DNC ratios found in the HMC stage, suggesting another possible formation route. The HCN/HNC median ratios is between 0.4 – 1.4 in the different stages and slightly increases with stage. This is consistent within the observational uncertainties with theoretical expectations of the ratio of 1 in cold clouds and  $> 1$  in warmer clouds (Sarrasin et al. 2010).

### 6.2. Relation between deuteration and other parameters

We measured the full width at half maximum (FWHM) of HCN, HN<sup>13</sup>C, H<sup>13</sup>CO<sup>+</sup> and N<sub>2</sub>H<sup>+</sup>. The isotopologues are assumed to be optically thin. For N<sub>2</sub>H<sup>+</sup> and HCN we corrected the measured optically thick FWHM  $\Delta\nu_{\text{thick}}$  according to Phillips et al. (1979) using the relation:

$$\frac{\text{FWHM}_{\text{thick}}}{\text{FWHM}_{\text{thin}}} = \frac{1}{\sqrt{\ln 2}} \sqrt{\ln \frac{\tau}{\ln \frac{2}{\exp(-\tau)+1}}} \quad (4)$$

where  $\tau$  is the optical depth of the line center and  $\text{FWHM}_{\text{thin}}$  the optically thin FWHM. We test for linear relationships using the Pearson correlation coefficient. By definition, the absolute value of  $\rho$  is  $\leq 1$  with a stronger correlation for larger  $\rho$ .  $\rho = 0$  means no correlation. The sign indicates a positive or negative correlation between the two quantities. In order to estimate  $\rho$  we randomly draw several times a set of data points from the measured values with their corresponding errors as well as the upper limits, and find for each of these drawn data sets the underlying correlation coefficient. We then find the most frequent correlation coefficient among all data sets as well as its 16% and 84% confidence values (Bailer-Jones et al. in prep.). The correlation plots are shown in Figure 7 and the corresponding Pearson correlation coefficients  $\rho$  are given in Table 3. The plots show that earlier phases have smaller FWHM.

The resulting coefficient is consistent with the data being uncorrelated for all four molecules. The FWHM of N<sub>2</sub>H<sup>+</sup> might be an exception and correlated, but is still  $< 0.5$  and no conclusive answer can be given. Although the correlation with the FWHM is weak, the decrease of the deuterium ratio with increasing FWHM is consistent with the picture of more quiescent, early stages with lower FWHM and higher deuteration fractions followed by more turbulent stages with higher FWHM and lower deuterium ratios.

Furthermore, we studied the correlation of the deuteration with the H<sub>2</sub> column density and luminosity  $L$ . The luminosities and H<sub>2</sub> column densities are shown in Tables A.2–A.3 and the corresponding correlation plots in Figure 8 and Figure 9. In general, the deuteration fraction shows similarly weak correlations with the luminosities as with the FWHM. Clearly, there is a lack of correlation with H<sub>2</sub> column densities. Among the four deuteration fractions, the strongest correlation is found for N<sub>2</sub>D<sup>+</sup>, but the correlation is still very low. The luminosity of a source is not necessarily a tracer of its evolutionary stage, but Figure 8 shows that the four different evolutionary stages are approximately separated with respect to the luminosity. Taking into account that the temperature of the objects increases with evolutionary stage, the luminosity can be used as a proxy for the temperature in the case of our source sample. Since higher luminosities indicate higher temperatures and smaller regions with  $T \lesssim 20$  K, where CO is frozen out, it reduces the overall abundance as well as the D/H ratio of N<sub>2</sub>H<sup>+</sup>. Among all four molecular deuteration fractions, DCN and DCO<sup>+</sup> show the weakest correlation with any of the shown parameters. However, none of the studied correlations have correlation coefficients  $\rho > 0.5$ .

### 6.3. Modeling the chemical evolution

With the observed column densities of 18 species (14 from Paper I) including 4 deuterated species in different stages of massive star formation at hand, we applied the iterative physico-chemical fitting model “MUSCLE-D” (“MULTI Stage CLOUD code with D-chemistry”) to these data. A list of all fitted species is given in Table 4. The model fits the evolution of the observed chemical data and thereby constrains basic physical properties in the assumed evolutionary path of high-mass star formation, such as mean temperatures and mean chemical ages. The chemical ages can be interpreted as typical lifetimes of the various stages. This model is the extended version of the iterative fitting model “MUSCLE” (“MULTI Stage CLOUD code”) already used and described in Gerner et al. (2014) and includes a physical and a chemical model. Here we will give a short summary of the main



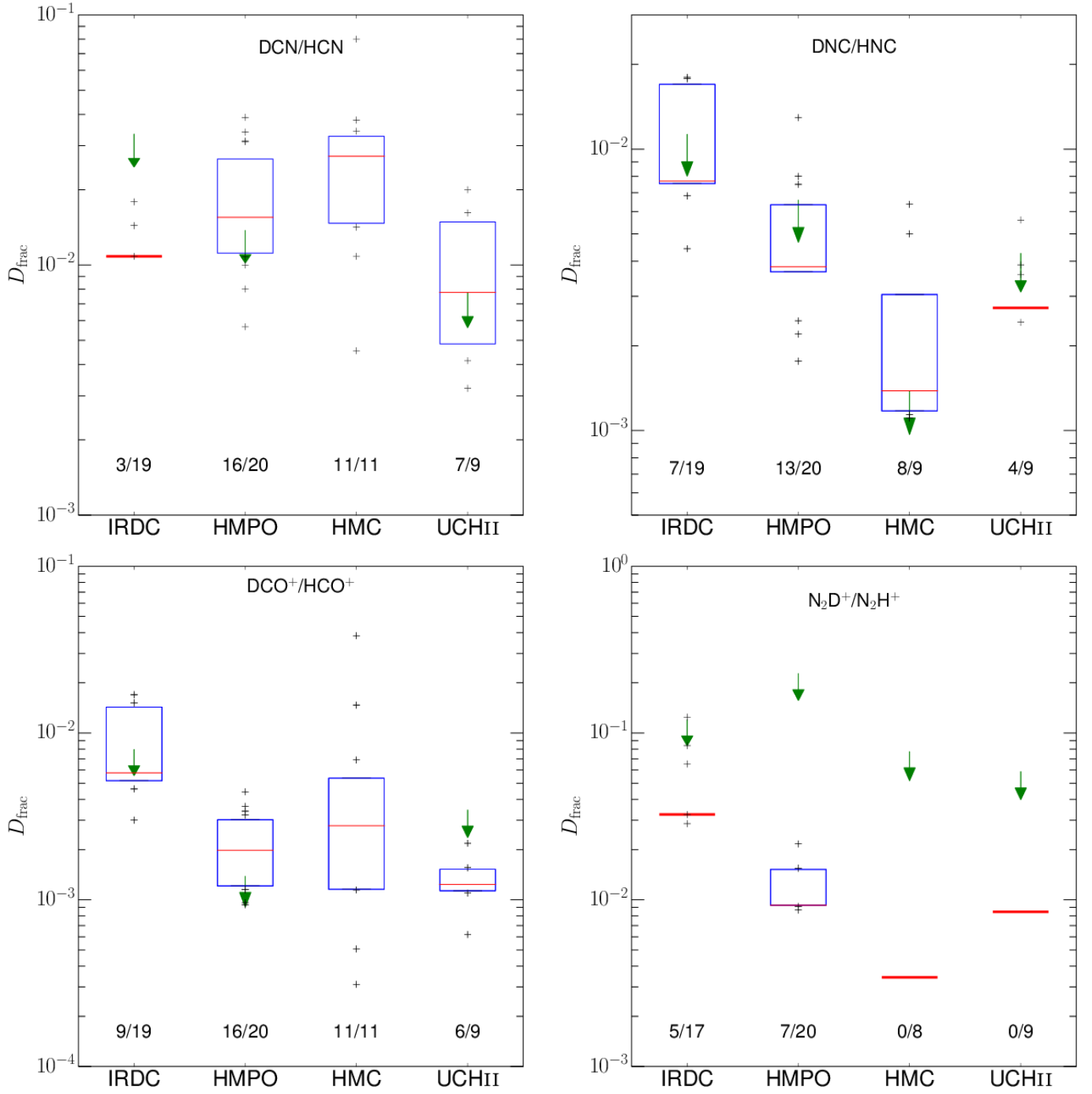


**Fig. 5.** Spread in deuteration fractions  $D_{\text{frac}}$  among the 4 evolutionary stages for HCN, HNC, HCO<sup>+</sup> and N<sub>2</sub>H<sup>+</sup>. In cases of 6 or more detections within one stage, the blue box shows the 25%-75% range and the crosses mark the remaining 50% of the data points. In cases of less than 6 data points, only the individual data points are shown. The red solid line shows the median of all detections and upper limits. The downward arrow shows the maximum value of all upper limits within that stage. The fractions at the bottom of each stage give the detection rate.

**Table 3.** Correlation coefficients  $\rho$  with 16% and 84% confidence values.

	Luminosity	N(H <sub>2</sub> )	FWHM
DCO <sup>+</sup> /HCO <sup>+</sup>	-0.21 <sup>0.02</sup> <sub>-0.35</sub>	0.03 <sup>0.49</sup> <sub>-0.31</sub>	-0.05 <sup>0.06</sup> <sub>-0.21</sub>
DCN/HCN	0.19 <sup>0.23</sup> <sub>0.01</sub>	-0.07 <sup>0.23</sup> <sub>-0.13</sub>	0.09 <sup>0.26</sup> <sub>-0.03</sub>
DNC/HNC	-0.27 <sup>-0.14</sup> <sub>-0.36</sub>	-0.01 <sup>0.13</sup> <sub>-0.15</sub>	-0.23 <sup>-0.13</sup> <sub>-0.32</sub>
N <sub>2</sub> D <sup>+</sup> /N <sub>2</sub> H <sup>+</sup>	-0.47 <sup>-0.14</sup> <sub>-0.51</sub>	-0.05 <sup>0.04</sup> <sub>-0.14</sub>	-0.43 <sup>-0.26</sup> <sub>-0.47</sub>



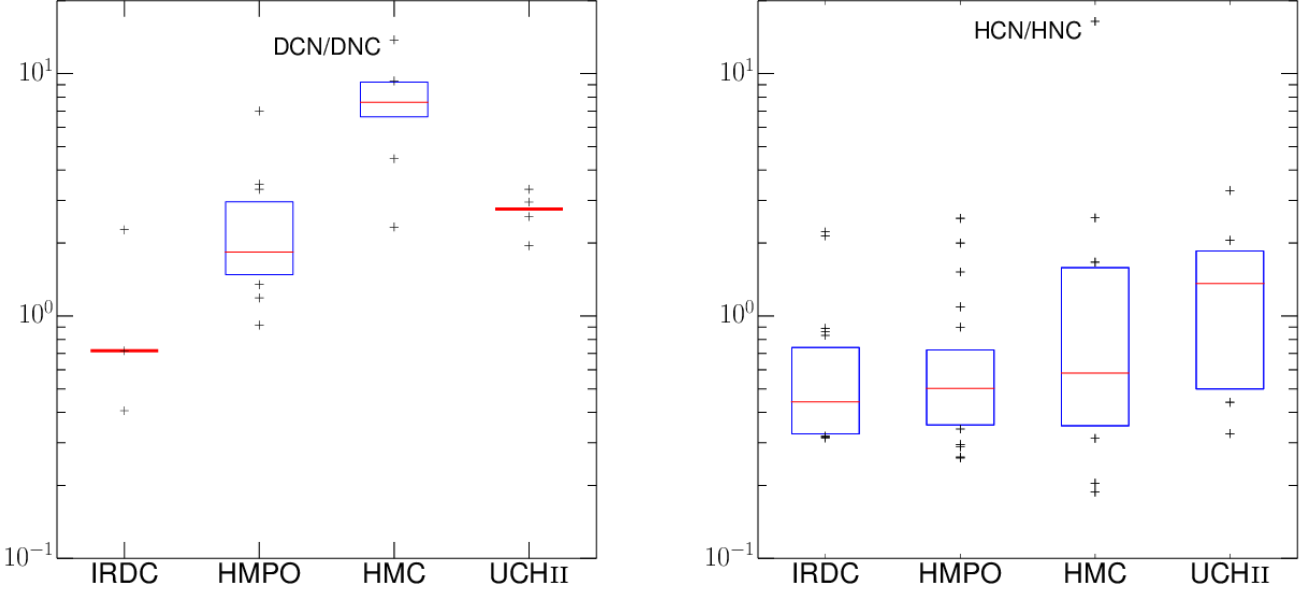


**Fig. 6.** Spread in fractions among the 4 evolutionary stages for DCN/DNC and HCN/HNC for detections in both molecules only. In case of 6 or more detections within one stage, the blue box shows the 25%-75% range and the crosses mark the remaining 50% of the data points. In cases of less than 6 data points, only the individual data points are shown. The red solid line shows the median of the ratio of detections in both molecules.

**Table 4.** List of species fitted with the model.

Molecules
CO <sup>a</sup> , HNC <sup>a</sup> , HCN, HCO <sup>+</sup> , HNCO, H <sub>2</sub> CO, N <sub>2</sub> H <sup>+</sup> , CS <sup>a</sup> , SO OCS, C <sub>2</sub> H, SiO, CH <sub>3</sub> CN, CH <sub>3</sub> OH, DCO <sup>+</sup> , DCN, DNC, N <sub>2</sub> D <sup>+</sup>
<sup>(a)</sup> Minor isotopologue observed

characteristics of the two parts of “MUSCLE-D”, the physical model in Section 6.3.1 and the chemical model “ALCHEMIC” in Section 6.3.2.

### 6.3.1. Physical model

The physical model treats the star-forming region as spherically symmetric 1D-clouds with a fixed outer radius of  $r_{\text{out}} = 0.5$  pc, based on the largest beam size of our observations of  $30''$  and the typical size of high-mass star forming regions. High angular resolution studies revealed in some of the sources complex structures that deviate from the spherically symmetric case (e.g., Beuther et al. 2002a). However, in single-dish maps these sources appear to be symmetric (e.g., Beuther et al. 2002b). Since we are analyzing single-dish data, a 1D-model physical model appears to be sufficient. More sophisticated models, that take into account complicated substructures, would increase the number of fitting parameters and might lead to an over-interpretation of the data. The radial density and temperature structure is modeled with

$$\begin{aligned} \rho(r) &= \rho_{\text{in}}(r/r_{\text{in}})^{-p}, & r \geq r_{\text{in}}; \\ \rho(r) &= \rho_{\text{in}}, & r < r_{\text{in}} \end{aligned} \quad (5)$$

and

$$\begin{aligned} T(r) &= T_{\text{in}}(r/r_{\text{in}})^{-q}, & r \geq r_{\text{in}}; \\ T(r) &= T_{\text{in}}, & r < r_{\text{in}}, \end{aligned} \quad (6)$$

respectively. The temperature and density profiles do not change with time. The fitted physical quantities are the inner radius  $r_{\text{in}}$ , the temperature and density at the inner radius,  $T_{\text{in}}$  and  $\rho_{\text{in}}$  and the power law index of the density  $p$ . The inner radius is limited between  $5 \times 10^{-5} - 5 \times 10^{-2}$  pc. While we assume the IRDC is an isothermal sphere, the temperature structure of the more evolved stages is modeled by a inner flat plateau with  $T_{\text{in}}$  and a power-law with slope  $q = 0.4$  as a standard value for  $r > r_{\text{in}}$  (see van der Tak et al. 2000). The radial density profile within  $r_{\text{in}}$  is flat with  $\rho_{\text{in}}$  and decreases for  $r > r_{\text{in}}$  as a power law with slope  $p$ . The value of  $p$  is limited to values between 1.5 and 2.0 in order to save computing time. That range is supported by several observations, e.g. Guertler et al. (1991); Beuther et al. (2002b); Mueller et al. (2002); Hatchell & van der Tak (2003). The temperature and density profiles are simultaneously fitted. The model does not take into account radiative transport. In the model, the whole cloud is embedded in a larger diffuse low-density medium that shields the high-mass star forming cloud from the interstellar FUV radiation.

### 6.3.2. Chemical model

The chemical model is an updated version of the time-dependent gas-grain chemical model “ALCHEMIC” described in Semenov et al. (2010) and already used and described in Gerner et al. (2014). In addition, the deuterium network from Albertsson et al. (2013) was added and extended with high-temperature reactions (Harada et al. 2010, 2012; Albertsson et al. 2014b) and ortho/para states of H<sub>2</sub>, H<sub>2</sub><sup>+</sup> and H<sub>3</sub><sup>+</sup> and their isotopologues (Albertsson et al. 2014a). In total, the chemical network comprises

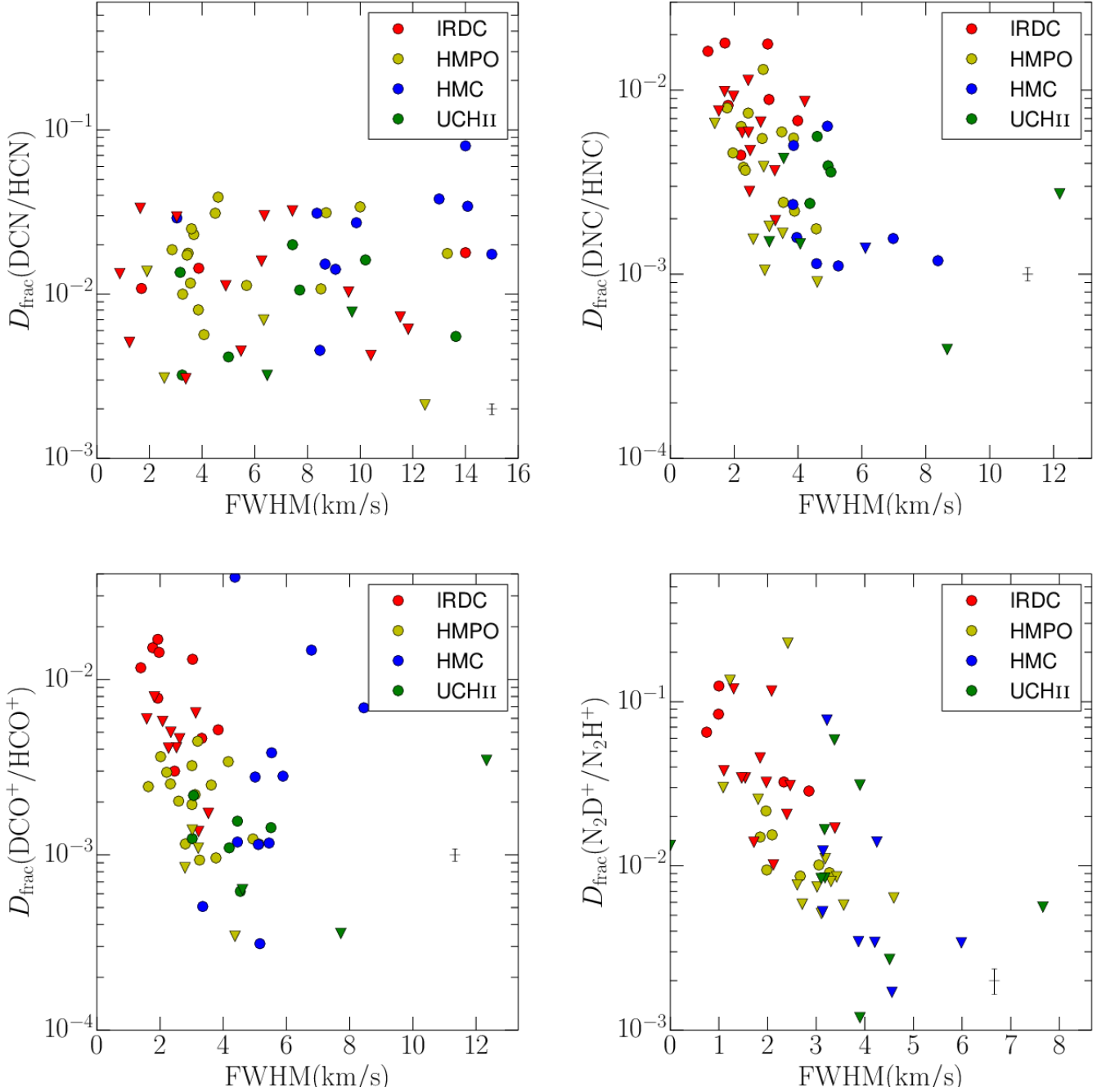


**Fig. 7.** Deuteration fractions of HCN, HNC,  $\text{HCO}^+$  and  $\text{N}_2\text{H}^+$  vs. FWHM of non-deuterated species from HCN (or  $\text{H}^{13}\text{CN}$  in case HCN is not available),  $\text{HN}^{13}\text{C}$ ,  $\text{H}^{13}\text{CO}^+$  and  $\text{N}_2\text{H}^+$ , respectively. The dots mark detections, the triangles upper limits. The typical size of an error bar from the uncertainty in the integrated flux is given in the lower right.

15 elements that can form 1260 different species from 38 500 reactions.

The initial abundances prior to the IRDC stage are taken from the “low metals” set given in Lee et al. (1998) with changed elemental abundance of Si ( $3 \times 10^{-9}$  with respect to H) and S ( $8 \times 10^{-7}$  with respect to H). The changes were needed in order to achieve proper fits to the IRDC phase. Initially, all metals (C, O, N, S, etc.) are in atomic form. Only  $\text{H}_2$  is already in molecular form. The initial ortho-para ratio of  $\text{H}_2$  is assumed to be the statistical value of 3:1. The model includes nuclear spin state exchange reactions to account for the evolution of the ortho-para

ratio as well as freeze out of CO. For the subsequent stages, the chemical outcome of the previous best-fit model is used as input initial abundances.

### 6.3.3. The fitting procedure

The fitting for the different stages is done iteratively using the physical and chemical model described above. In this sense we modeled the observed column densities for the IRDC, HMPO and HMC stage by varying the parameters  $r_{\text{in}}$ ,  $T_{\text{in}}$ ,  $\rho_{\text{in}}$  and  $p$ . While keeping all other parameters fixed, we vary these four

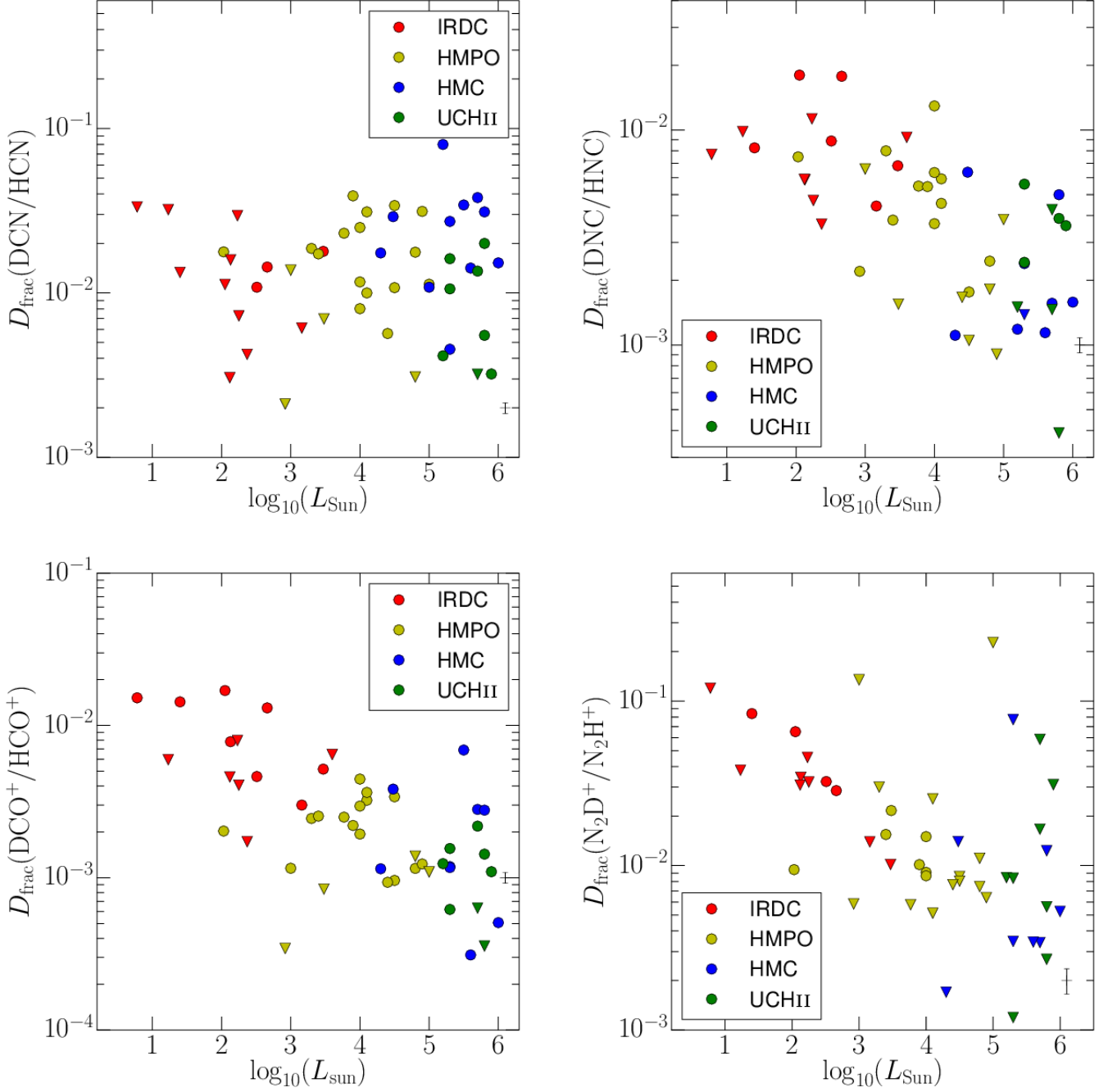


**Fig. 8.** Deuteration fractions of HCN, HNC, HCO<sup>+</sup> and N<sub>2</sub>H<sup>+</sup> vs. the luminosity of the source. The dots mark detections, the triangles upper limits. The typical size of an error bar from the uncertainty in the integrated flux is given in the lower right.

parameters and run the model over  $10^5$  yr for each of the realizations. Then we compute the  $\chi^2$ -value for each time step and model realization, given the observed mean column densities and computed model column densities. We assumed the standard deviation between modeled and observed values to be one order of magnitude as a typical value. Molecules that were detected in less than 50% of the sources within one stage were considered as upper limits. Finally, the model with the minimum  $\chi^2$ -value is found as the best-fit model which matches best with the calculated mean column densities for each stage.

Due to the iterative fitting along the evolutionary sequence, the introduced uncertainties increase with evolutionary stage

leading to a limited confidence in the obtained results for the later stages.

#### 6.4. The modeling results

We fitted the combined data from Gerner et al. (2014) and this work with the above described model assuming an ortho-para H<sub>2</sub> ratio o/p=3:1. The resulting best-fit model parameters for the IRDC, HMPO, HMC and UCHII stage are shown in Tables A.4 – A.7. The evolution of the best-fits with time is shown in Figure 10. These distributions give a good sense of the uncertainty of the chemical age. The best-fit lifetime is 16 500 years for

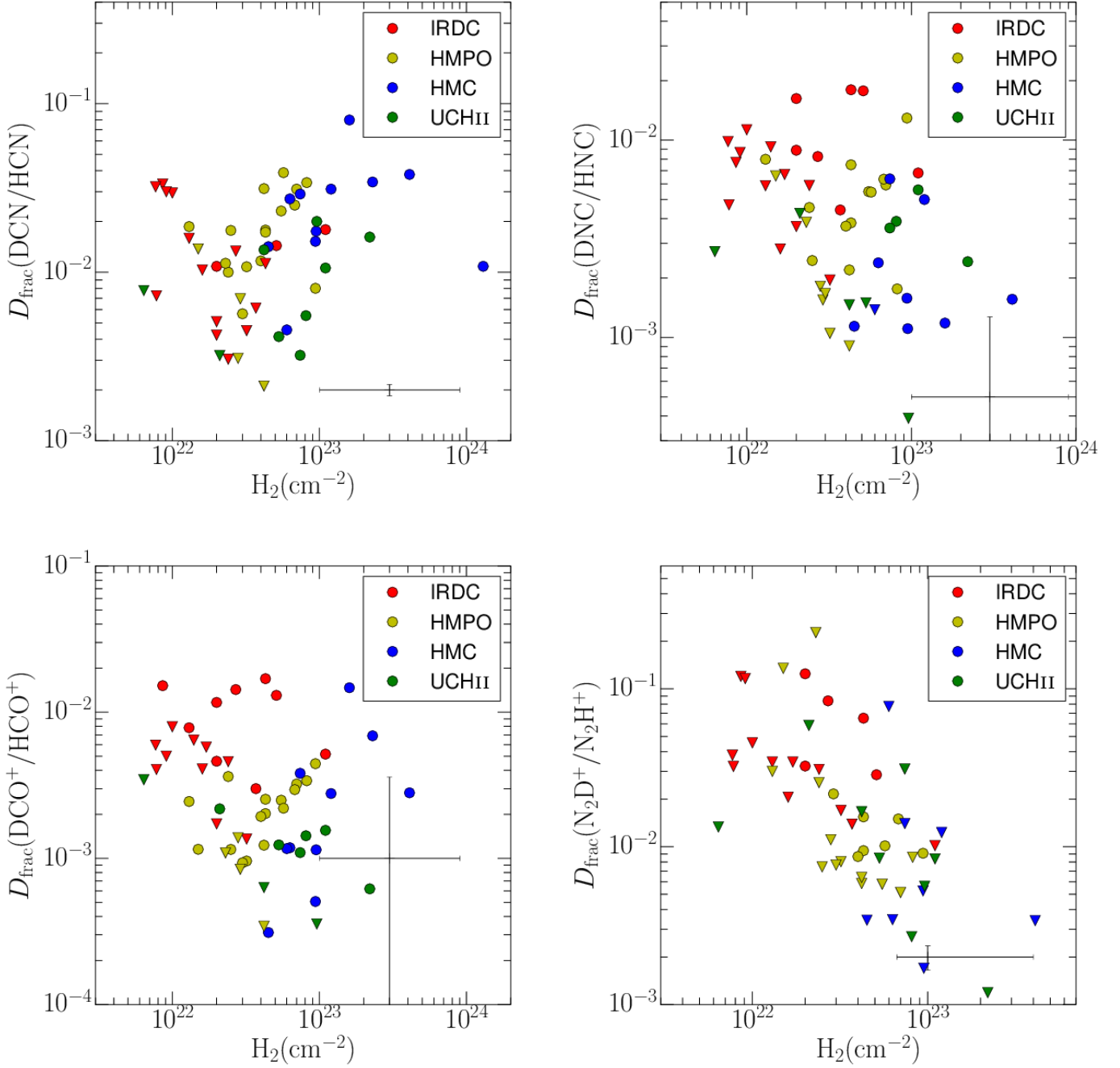


**Fig. 9.** Deuteration fractions of HCN, HNC,  $\text{HCO}^+$  and  $\text{N}_2\text{H}^+$  vs. the  $H_2$  column density of the source. The typical size of an error bar from the uncertainty in the integrated flux and from the uncertainty in the derived  $H_2$  column densities (see Section A.1) is given in the lower right.

the IRDC stage. A good fit was also achieved with a chemical age of only 1,000 years. However, that seems to be a rather short timescale and might be interpreted as a lower limit. The HMPO best-fit age yielded 32 000 years with likely values between 10 000 – 40 000 years. For the HMC stage we found a best-fit age of 35 000 years with values below 15 000 years being unlikely. The best-fit age for the UCHII stage was found rather short with 3 000 years, but quite unconstrained with likely values up to several 10 000 years.

The observed and modeled column densities are shown in Tables A.8 – A.11. The best-fit of the IRDC stage reproduces 18 of 18 molecules within the assumed combined (observational +

chemical) uncertainty of one order of magnitude. In the HMPO stage the model is able to reproduce 16 of 18 molecules. SO is overproduced by a factor of  $\sim 20$  and  $\text{CH}_3\text{OH}$  underproduced by a factor of  $\sim 40$ . The underproduction of methanol is possibly due to shock- or outflow-triggered enhanced desorption of methanol ice from grains, which is not taken into account in the model. The reason for the misfit of SO might be a poorly understood chemistry of sulfur-bearing species in modern astrochemical models in general. In the HMC stage the model could fit 14 of 18 species. Besides  $\text{C}_2\text{H}$ , which is  $\sim 20$  times underproduced,  $\text{HNCO}$ , SO and  $\text{CH}_3\text{OH}$  are misfitted by more than a factor of 100. The underproduction of  $\text{CH}_3\text{OH}$  and overproduction of SO

in the HMPO stage is continuing in the HMC phase. The overproduction of HNCO might be connected to not well enough understood shock- and surface chemistry. This difference in  $C_2H$  between the model and observations might be influenced by UV-radiation of the central star(s) or a clumpy structure of the environment, which is not considered in the model. That is especially important for the UCH<sub>II</sub> regions, but it is also already present in some HMCs. For the last considered stage of an UCH<sub>II</sub> region the model reproduces 13 of 18 species. As in the HMC stage, the molecules HNCO, SO and  $C_2H$  are misfitted in the UCH<sub>II</sub> stage. In addition, SiO and  $DCO^+$  are slightly overproduced.

In general, the overall fit of all 18 molecules of the four fitted phases is good. The specific time dependent evolution of the best-fit abundances of molecules DCN, DNC,  $DCO^+$ ,  $N_2D^+$  and their non-deuterated counterparts are shown in Figure 11. Between two consecutive stages, the physical parameters are instantly changed and the molecular species show a quick response to that change, followed by a slower evolution under the new constant conditions. Figures A.1–A.4 show the modeled column densities in each stage separately. In total the best-fit ages add up to 85,000 years, which is on the same order as typical models of high-mass star formation of  $10^5$  years (e.g., McKee & Tan 2003; Tan et al. 2014).

The evolution for the different molecular ratios are shown in Figure 12. The modeled abundance ratios show partly larger deviations from the observed values, since the uncertainties from both molecules add up. In Sect. 6.1 we discussed the ratio of DCN/DNC and a possible chemical explanation based on a chemical network by Turner (2001). However, the chemical network used in our work shows a different trend with a constant ratio rather than an increase of DCN/DNC with temperature. Thus the observed trend disagrees with our model predictions and the possibility of different chemical formation pathways needs to be tested by future observations of more deuterated molecules sharing the same formation pathways as DCN (e.g., light hydrocarbons with 2 or 3 C-atoms). The model agrees with the constant ratio of HNC/HCN of unity with recent developments in the collisional rates by Sarasin et al. (2010).

### 6.5. Comparison with best-fit models of Paper I

In Paper I we iteratively fitted our model to an observational dataset containing the median column densities of 14 different non-deuterated species. The column densities were derived with typical temperatures for each stage. The model followed the observed evolution and successfully fit most of the species with few exceptions in individual stages. The fits also constrained the physical structure of the model and yielded mean best-fit temperatures for each stage. The mean temperatures deviated from the temperatures used to derive the observed column densities for the later stages. In a second step we fitted the newly derived column densities. The temperature in the best-fit models decreased again and we could not find a converging solution.

In this work we used the best-fit temperatures of the first model from Paper I to recalculate the median column densities for the previously analyzed 14 species and additional four deuterated species. The temperature in the best-fit model of the IRDC stage is lower by a factor of 2 compared to Paper I, but the best-fit temperatures of the IRDC stage for both, Paper I and this work, agree with typical IRDC temperatures. The mean density increased about an order of magnitude. The best-fit lifetime in this work is a factor of 1.5 longer, but agrees within the assumed uncertainties. The HMPO best-fit mean temperature in this work is lower by 30%. The mean density increased by a factor 3 – 4.

The best-fit lifetime is shorter by a factor of  $\sim 2$ . The HMC best-fit mean temperature in this work is higher by 25%. The mean densities are similar. In comparison to Paper I, the best-fit lifetime is about 20% lower. The UCH<sub>II</sub> best-fit mean temperatures are similar. The best-fit ages deviate by a factor of 4, but are consistent within their likely ranges. The mean density is smaller by one order of magnitude.

The total lifetimes from the IRDC to the UCH<sub>II</sub> phase in Paper I adds up to  $\sim 110,000$  years. This work yields a total lifetime that is slightly shorter with  $\sim 85,000$  years. The molecules that could not be reproduced in Paper I and this work are not the same. Possible reasons are the additional four deuterated molecules as free fit parameters that were treated with equal weight as well as the revised excitation temperatures in order to derive column densities compared to Paper I (see Section 5.2). Although D-chemistry is seen as a tracer of the thermal history and conditions of an object, and we see weak correlations with luminosity as an evolutionary tracer, the model fits did not improve substantially. Increasing the number of fitted molecules from 14 to 18 species did not improve the achieved results strongly, probably due to the less statistical importance of the deuterated molecules within the total number of 18 species.

### 6.6. Comparison with literature

In low-mass star formation both observations and theory show that it is possible to use the deuteration fraction of a molecule as an evolutionary tracer (e.g., Crapsi et al. 2005; Aikawa et al. 2005; Emprechtinger et al. 2009). In a recent work, Fontani et al. (2011) observed 27 cores within high-mass star-forming regions and derived the deuteration fraction of  $N_2D^+/N_2H^+$ . They found a similar behavior as in the low-mass regime. The deuteration fraction is the highest in the starless cores with  $D_{\text{frac}} = 0.26$  and decreases during the formation of the protostellar objects to  $D_{\text{frac}} = 0.04$ . We find in our work a similar trend, but the median deuteration fraction we measure in our IRDC sample is lower by a factor of four compared to their high-mass starless core sample. That might be due to the fact that our IRDC sample contains starless as well as already more evolved objects inhabiting  $24\mu\text{m}$  sources. The same is true for the HMPO samples of Fontani et al. (2011) and this work. We find lower ratios by about a factor of four. The largest D/H ratio we see is the  $N_2D^+/N_2H^+$  ratio in IRDC20081 of  $D_{\text{frac}} = 0.12$ . This source inhabits no point sources below  $70\mu\text{m}$ , but it is close to a nearby source with extended emission. It is presumably in a very early pre-stellar phase. Miettinen et al. (2011) studied seven massive clumps within IRDCs and derived deuteration fractions for  $N_2H^+$  between 0.002–0.028 and for  $HCO^+$  between 0.0002 – 0.014. While the range of values for  $HCO^+$  is comparable with the IRDCs in our sample, the deuteration fractions for  $N_2H^+$  are about one order of magnitude higher in this work. However, that agrees with the high number of upper limits due to non-detections of  $N_2D^+$  in this work. Chen et al. (2011) observed several cores in various evolutionary stages and found deuteration values of  $N_2H^+$  between 0.004 – 0.1. The source lists have three targets in common. For the HMPO18151 both works agree on a value of  $D_{\text{frac}} = 0.01$ . For the other two sources in common, IRDC18151 and IRDC18223, we find a slightly higher value of  $D_{\text{frac}} = 0.03$  instead of  $D_{\text{frac}} = 0.02$ . While the highest value they found is similar to the maximum value we observe, they detected  $N_2D^+$  in a larger number of sources and found also lower deuteration fractions, especially in the more evolved sources for which we have no detections of  $N_2D^+$ . Work by Crapsi et al. (2005) studying the  $N_2D^+/N_2H^+$  ratio in low-mass starless cores

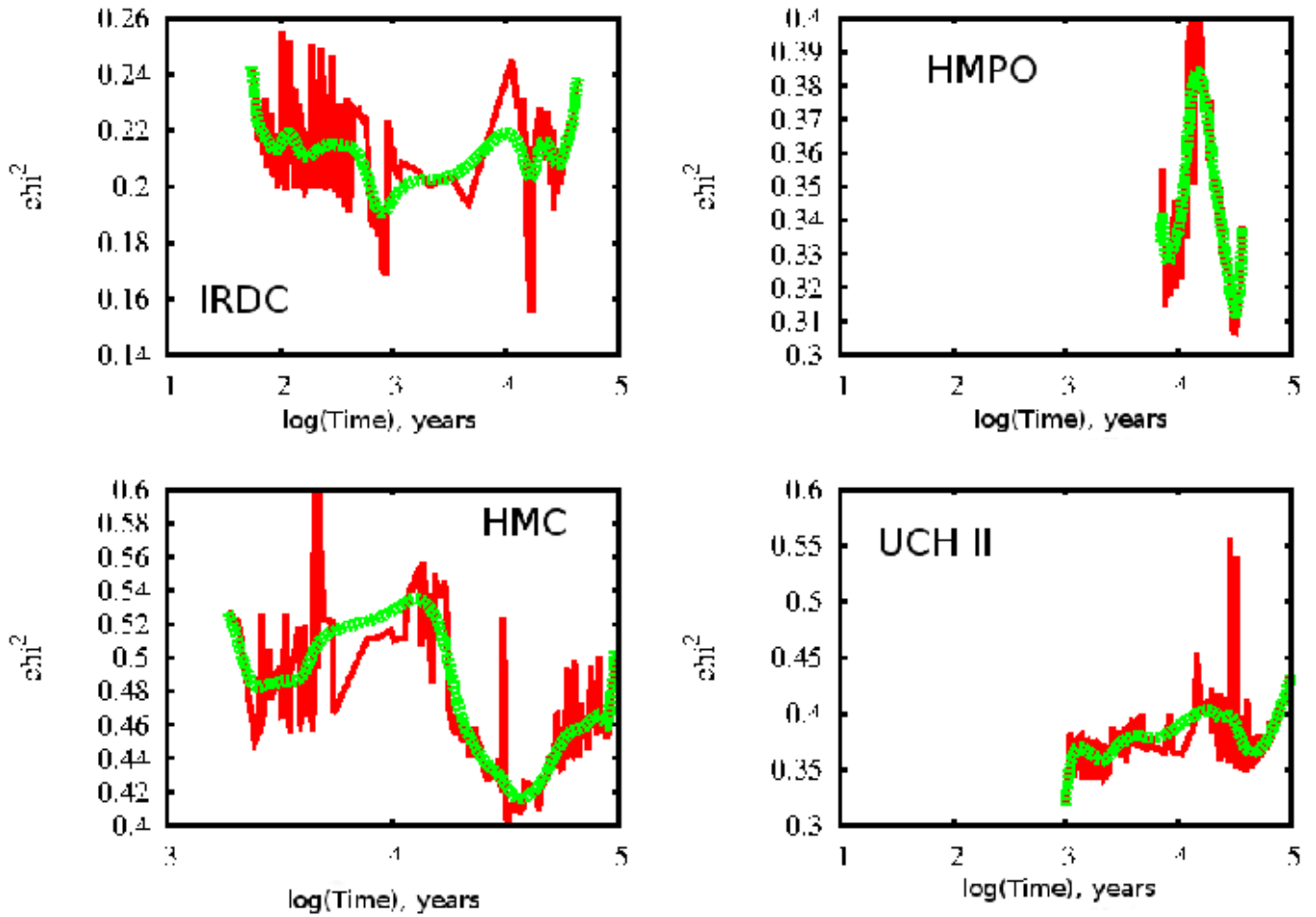


**Fig. 10.** Evolution of the minimum  $\chi^2$  of the best-fit models with time. The four panels show the four different stages IRDC (upper left), HMPO (upper right), HMC (lower left) and UCH II (lower right). The red curve marks the calculated values at all 299 time moments, whereas the green curve shows their smoothed spline interpolation.

revealed deuteration fractions on the percentage level up to almost 50% in the most extreme case of Oph D. The maximum ratio observed in our survey is  $\sim 0.1$ . Sakai et al. (2012) measured deuteration fractions of DNC/HNC for IRDCs and HMPOs. They find  $D_{\text{frac}} = 0.003 - 0.03$  for MSX (Midcourse Space Experiment) dark sources at  $8\mu\text{m}$  and  $D_{\text{frac}} = 0.005 - 0.01$  for HMPOs. These ratios agree well with  $D_{\text{frac}} = 0.004 - 0.02$  for our IRDC sample and  $D_{\text{frac}} = 0.0015 - 0.015$  for our HMPO sample. In a recent study, Kong et al. (2013) explored the effect of different parameters on the deuteration fraction of  $\text{N}_2\text{H}^+$  in dense and cold environments. They found an increase of the deuteration fraction with decreasing temperature. However, they also found a positive correlation with the density, which is not clearly seen in our data. They employed a 0D model to study deuteration in star-forming clouds and found that the timescales to reach equilibrium in the abundances is on the order of several free-fall times ( $\sim 10^6$  years) for typical densities of high-mass cores. In contrast, the best-fit models in our work are not supposed to reach chemical equilibrium and thus our model predicts a total timescale of  $\sim 10^5$  years for the best-fit models. This is likely due to the fact that in a 1D model with a power law density profile with higher densities in the inner region timescales in the chemical evolution are shorter than in a 0D model.

## 7. Conclusion

In this work we extended the analysis from Gerner et al. (2014) of the chemical evolution in 59 high-mass star forming regions for deuterated molecules. We measured beam averaged column densities and deuteration fractions of the four deuterated species  $\text{DCO}^+$ ,  $\text{DCN}$ ,  $\text{DNC}$ , and  $\text{N}_2\text{H}^+$ . We find an overall high detection fraction towards the high-mass star-forming regions, except for  $\text{N}_2\text{D}^+$ , which is likely due to the limited sensitivity of our survey. The detection fraction of  $\text{DCO}^+$ ,  $\text{DCN}$  and  $\text{DNC}$  increases from IRDCs to HMPOs and peaks at the HMC sample, where we detect all three molecules in all sources but one, and drops again towards the UCH II stage.

The (3-2) lines are sub-thermally populated. The median deuteration fractions excluding upper limits are 0.02 for  $\text{DCN}$ , 0.005 for  $\text{DNC}$ , 0.0025 for  $\text{DCO}^+$  and 0.02 for  $\text{N}_2\text{D}^+$ . The deuteration fractions of  $\text{DNC}$ ,  $\text{DCO}^+$  and  $\text{N}_2\text{D}^+$  show a decreasing trend from IRDCs over HMPOs and HMCs to UCH II regions, which supports the hypothesis that deuterated molecules may be used as indicators of the evolutionary stage in high-mass star-forming regions.

In general, we find no correlation between the deuteration fraction of the various molecules and physical parameters for  $\text{DCO}^+/\text{HCO}^+$  and  $\text{DCN}/\text{DNC}$ . Only  $\text{N}_2\text{D}^+/\text{N}_2\text{H}^+$  shows a slight anti-correlations with the luminosity and the FWHM. The to-

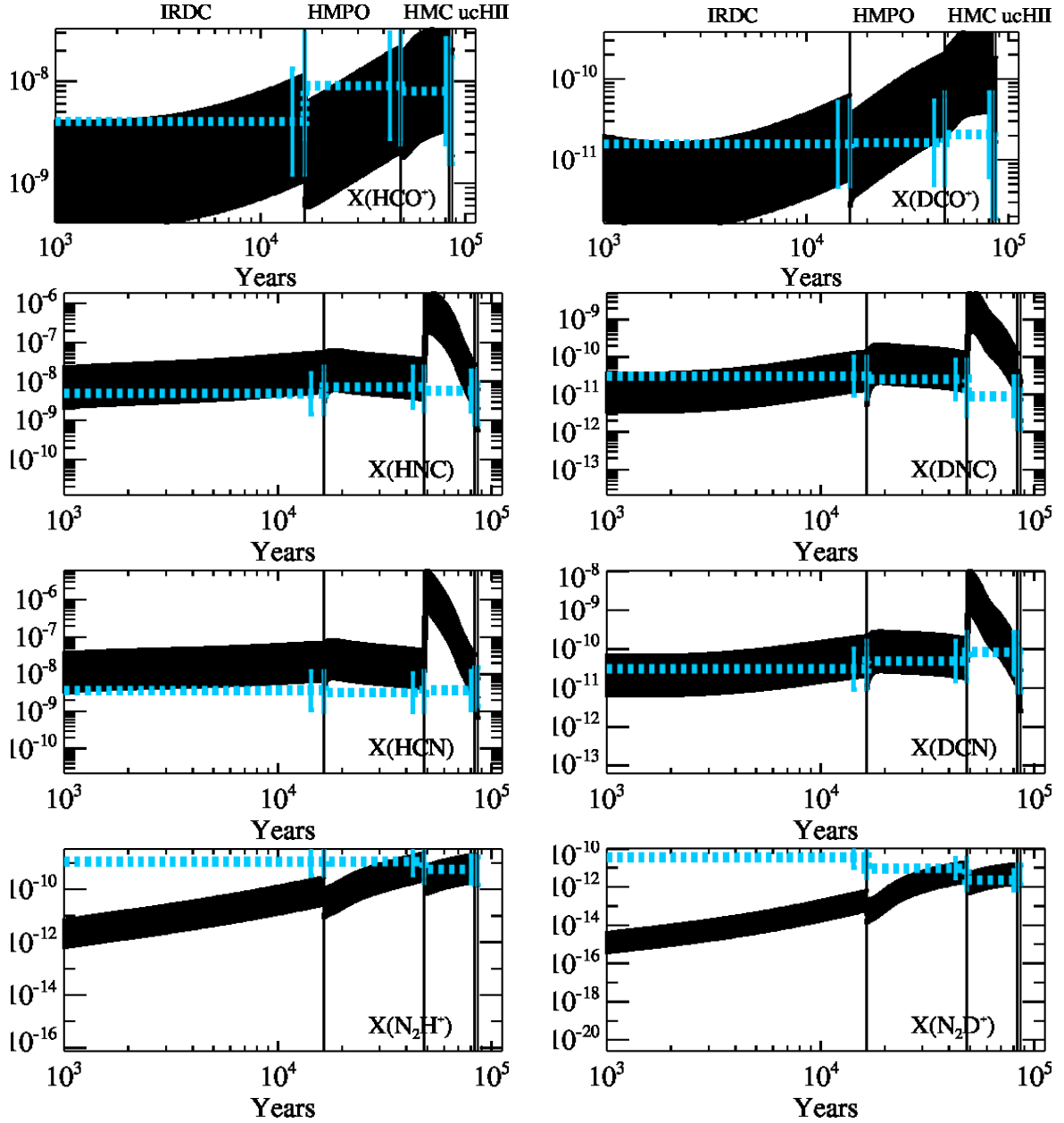


**Fig. 11.** Modeled and observed relative abundances to  $\text{H}_2$  are plotted for the IRDC-UCHII stages. The modeled values are shown by the black solid line, the observed values show the median of all detections and upper limits and are depicted by the blue dashed line. The error bars are indicated by the vertical marks.

tal measured column density of the gas does not correlate with the deuteration fraction. This result hints towards the interpretation that, within the range of probed densities, deuteration depends stronger on the temperature of the environment than on the column density, and is enhanced in colder, less luminous regions. However, for example Albertsson et al. (2013) found in their models differences in the deuteration with density at lower densities.

The slight anti-correlation with luminosity and FWHM, which is related to the evolutionary stage, indicates that evolutionary stage plays an important role for the deuteration fraction. But its huge scatter within single stages leads to the assumption that the evolution might not be the only factor.

Furthermore, we fitted the observed data with a chemical model and find reasonable physical model fits. Combining observations of non-deuterated and deuterated species to obtain

best-fits lead to reasonable chemical and physical models. The best-fit models produce reasonably good results for all stages. Due to large uncertainties in the observations and the model and a large spread of observed values within the 4 subsamples we could not substantially improve the best-fit model results compared to Paper I. Another reason is that the combination of the 4 deuterated molecules with the 14 non-deuterated species probably reduced the statistical importance of each molecule and thus the effect on the best-fit of the model.

*Acknowledgements.* The authors thank the anonymous referee for helping to improve the paper. TG is supported by the Sonderforschungsbereich SFB 881 ‘The Milky Way System’ (subproject B3) of the German Research Foundation (DFG). T.G. is member of the IMPRS for Astronomy & Cosmic Physics at the University of Heidelberg. This research made use of NASA’s Astrophysics Data System. DS acknowledges support by the *Deutsche Forschungsgemeinschaft* through SPP 1385: “The first ten million years of the solar system - a planetary materials approach” (SE 1962/1-2 and SE 1962/1-3). TA ac-



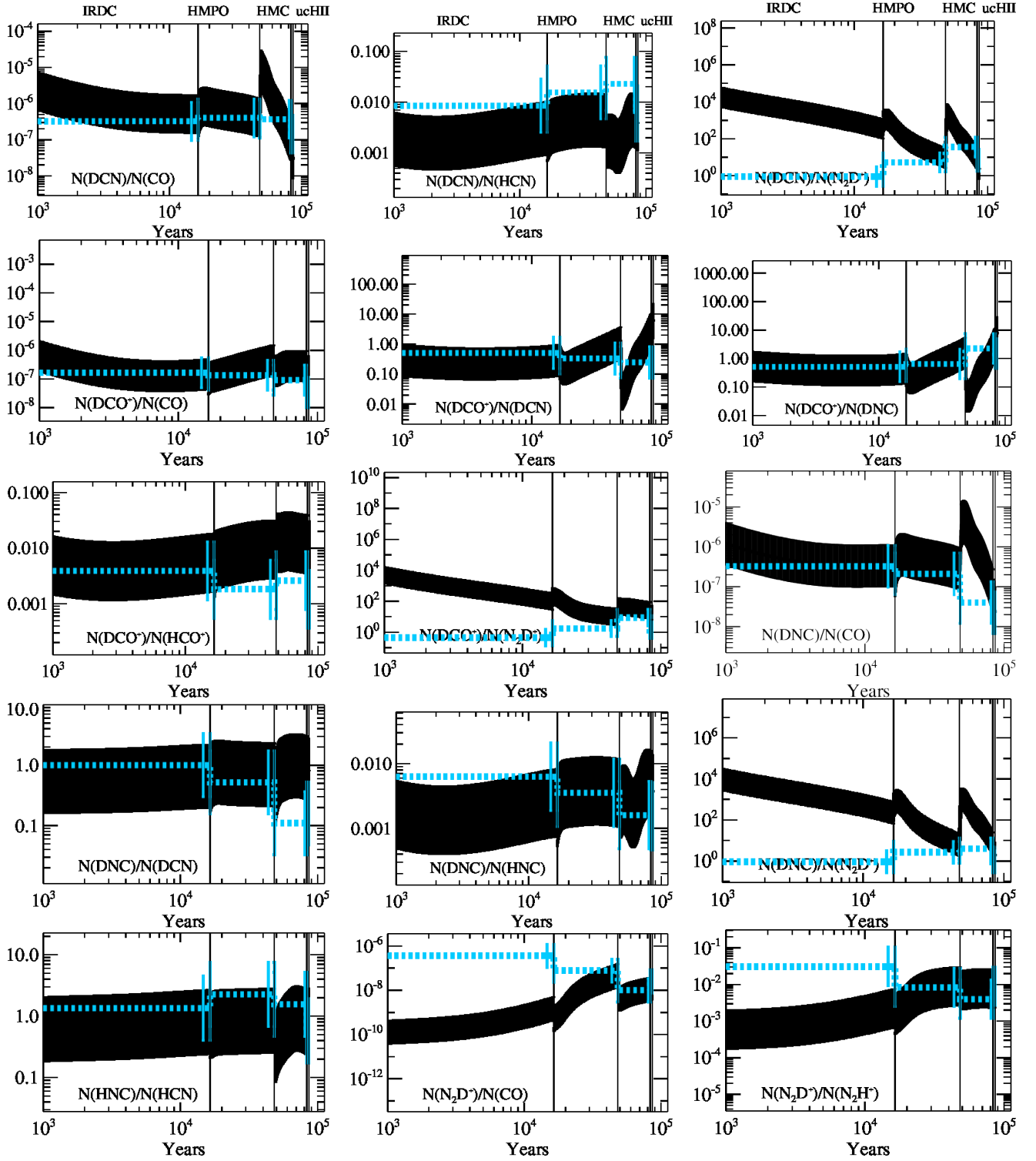


**Fig. 12.** Modeled and observed column density ratios are plotted for all stages. The modeled values are shown by the black solid line, the observed values show the median of all detections and upper limits and are depicted by the blue dashed line. The error bars are indicated by the vertical marks.

knowledge funding from the European Community's Seventh Framework Programme [FP7/2007-2013] under grant agreement no. 238258. In the reduction and analysis of the data we made use of the GILDAS software public available at <http://www.iram.fr/IRAMFR/GILDAS>. The SMT and Kitt Peak 12m are operated by the Arizona Radio Observatory (ARO), Steward Observatory, University of Arizona, with support through the NSF University Radio Observatories program (URO: AST-1140030).

## References

- Aikawa, Y., Herbst, E., Roberts, H., & Caselli, P. 2005, *ApJ*, 620, 330
- Albertsson, T., Indriolo, N., Kreckel, H., et al. 2014a, *ArXiv e-prints*
- Albertsson, T., Semenov, D., & Henning, T. 2014b, *ApJ*, 784, 39
- Albertsson, T., Semenov, D. A., Vasyunin, A. I., Henning, T., & Herbst, E. 2013, *ApJS*, 207, 27
- Barnes, P. J., Yonekura, Y., Fukui, Y., et al. 2011, *ApJS*, 196, 12
- Beuther, H., Churchwell, E. B., McKee, C. F., & Tan, J. C. 2007a, in *Protostars and Planets V*, ed. B. Reipurth, D. Jewitt, & K. Keil, 165–180

Beuther, H., Schilke, P., Gueth, F., et al. 2002a, *A&A*, 387, 931  
 Beuther, H., Schilke, P., Menten, K. M., et al. 2002b, *ApJ*, 566, 945  
 Beuther, H., Schilke, P., Sridharan, T. K., et al. 2002c, *A&A*, 383, 892  
 Beuther, H., Tackenberg, J., Linz, H., et al. 2012, *A&A*, 538, A11  
 Beuther, H., Zhang, Q., Bergin, E. A., et al. 2007b, *A&A*, 468, 1045  
 Beuther, H., Zhang, Q., Greenhill, L. J., et al. 2004, *ApJ*, 616, L31  
 Bourke, T. L., Myers, P. C., Caselli, P., et al. 2012, *ApJ*, 745, 117  
 Campbell, M. F., Butner, H. M., Harvey, P. M., et al. 1995, *ApJ*, 454, 831  
 Carey, S. J., Feldman, P. A., Redman, R. O., et al. 2000, *ApJ*, 543, L157  
 Caselli, P. & Ceccarelli, C. 2012, *A&A Rev.*, 20, 56  
 Caselli, P., Stantcheva, T., Shalabiea, O., Shematovich, V. I., & Herbst, E. 2002, *Planet. Space Sci.*, 50, 1257  
 Cesaroni, R., Churchwell, E., Hofner, P., Walmsley, C. M., & Kurtz, S. 1994, *A&A*, 288, 903  
 Chen, H.-R., Liu, S.-Y., Su, Y.-N., & Wang, M.-Y. 2011, *ApJ*, 743, 196  
 Chen, H.-R., Welch, W. J., Wilner, D. J., & Sutton, E. C. 2006, *ApJ*, 639, 975  
 Churchwell, E., Walmsley, C. M., & Cesaroni, R. 1990, *A&AS*, 83, 119  
 Crapsi, A., Caselli, P., Walmsley, C. M., et al. 2005, *ApJ*, 619, 379  
 Dalgarno, A. & Lepp, S. 1984, *ApJ*, 287, L47  
 Daniel, F., Cernicharo, J., Roueff, E., Gerin, M., & Dubernet, M. L. 2007, *ApJ*, 667, 980  
 Di Francesco, J., Johnstone, D., Kirk, H., MacKenzie, T., & Ledwosinska, E. 2008, *ApJS*, 175, 277  
 Emprechtinger, M., Caselli, P., Volgenau, N. H., Stutzki, J., & Wiedner, M. C. 2009, *A&A*, 493, 89  
 Fontani, F., Caselli, P., Crapsi, A., et al. 2006, *A&A*, 460, 709  
 Fontani, F., Palau, A., Caselli, P., et al. 2011, *A&A*, 529, L7  
 Friesen, R. K., Kirk, H. M., & Shirley, Y. L. 2013, *ApJ*, 765, 59  
 Gerner, T., Beuther, H., Semenov, D., et al. 2014, *A&A*, 563, A97  
 Guertler, J., Henning, T., Kruegel, E., & Chini, R. 1991, *A&A*, 252, 801  
 Harada, N., Herbst, E., & Wakelam, V. 2010, *ApJ*, 721, 1570  
 Harada, N., Herbst, E., & Wakelam, V. 2012, *ApJ*, 756, 104  
 Hatchell, J., Thompson, M. A., Millar, T. J., & MacDonald, G. H. 1998, *A&AS*, 133, 29  
 Hatchell, J. & van der Tak, F. F. S. 2003, *A&A*, 409, 589  
 Heitsch, F., Hartmann, L. W., Slyz, A. D., Devriendt, J. E. G., & Burkert, A. 2008, *ApJ*, 674, 316  
 Hiraoka, K., Ushiyama, S., Enoura, T., et al. 2006, *ApJ*, 643, 917  
 Kong, S., Caselli, P., Tan, J. C., & Wakelam, V. 2013, *ArXiv e-prints*  
 Lee, H.-H., Roueff, E., Pineau des Forets, G., et al. 1998, *A&A*, 334, 1047  
 Linsky, J. L. 2003, *Space Sci. Rev.*, 106, 49  
 Linz, H., Stecklum, B., Henning, T., Hofner, P., & Brandl, B. 2005, *A&A*, 429, 903  
 Lodders, K. 2003, *ApJ*, 591, 1220  
 Mangum, J. G. & Shirley, Y. L. 2015, *ArXiv e-prints*  
 McKee, C. F. & Tan, J. C. 2003, *ApJ*, 585, 850  
 Miettinen, O., Hennemann, M., & Linz, H. 2011, *A&A*, 534, A134  
 Millar, T. J., Bennett, A., & Herbst, E. 1989, *ApJ*, 340, 906  
 Mueller, K. E., Shirley, Y. L., Evans, N. J., & Jacobson, H. R. 2002, *ApJS*, 143, 469  
 Narayanan, D., Cox, T. J., Shirley, Y., et al. 2008, *ApJ*, 684, 996  
 Oliveira, C. M., Hébrard, G., Howk, J. C., et al. 2003, *ApJ*, 587, 235  
 Ossenkopf, V. & Henning, T. 1994, *A&A*, 291, 943  
 Parise, B., Leurini, S., Schilke, P., et al. 2009, *A&A*, 508, 737  
 Phillips, T. G., Huggins, P. J., Wannier, P. G., & Scoville, N. Z. 1979, *ApJ*, 231, 720  
 Pillai, T., Wyrowski, F., Hatchell, J., Gibb, A. G., & Thompson, M. A. 2007, *A&A*, 467, 207  
 Ragan, S., Henning, T., Krause, O., et al. 2012, *A&A*, 547, A49  
 Roberts, H. & Millar, T. J. 2000, *A&A*, 361, 388  
 Roueff, E., Parise, B., & Herbst, E. 2007, *A&A*, 464, 245  
 Sakai, T., Sakai, N., Furuya, K., et al. 2012, *ApJ*, 747, 140  
 Sarasin, E., Abdallah, D. B., Wernli, M., et al. 2010, *MNRAS*, 404, 518  
 Schöier, F. L., van der Tak, F. F. S., van Dishoeck, E. F., & Black, J. H. 2005, *A&A*, 432, 369  
 Schuller, F., Menten, K. M., Contreras, Y., et al. 2009, *A&A*, 504, 415  
 Semenov, D., Hersant, F., Wakelam, V., et al. 2010, *A&A*, 522, A42  
 Sridharan, T. K., Beuther, H., Saito, M., Wyrowski, F., & Schilke, P. 2005, *ApJ*, 634, L57  
 Sridharan, T. K., Beuther, H., Schilke, P., Menten, K. M., & Wyrowski, F. 2002, *ApJ*, 566, 931  
 Tan, J. C., Beltran, M. T., Caselli, P., et al. 2014, *ArXiv e-prints*  
 Testi, L., Hofner, P., Kurtz, S., & Rupen, M. 2000, *A&A*, 359, L5  
 Turner, B. E. 2001, *ApJS*, 136, 579  
 van der Tak, F. F. S., Black, J. H., Schöier, F. L., Jansen, D. J., & van Dishoeck, E. F. 2007, *A&A*, 468, 627  
 van der Tak, F. F. S., van Dishoeck, E. F., Evans, II, N. J., & Blake, G. A. 2000, *ApJ*, 537, 283  
 Watson, W. D. 1974, *ApJ*, 188, 35  
 Wilson, T. L. & Rood, R. 1994, *ARA&A*, 32, 191  
 Wood, D. O. S. & Churchwell, E. 1989a, *ApJ*, 340, 265  
 Wood, D. O. S. & Churchwell, E. 1989b, *ApJS*, 69, 831  
 Zinnecker, H. & Yorke, H. W. 2007, *ARA&A*, 45, 481

## Appendix A: Appendix material

### Appendix A.1: Molecular column densities

We calculated the molecular column densities of the upper level of a particular transition following the equation for optically thin emission:

$$N_u = \frac{8\pi k \nu^2}{hc^3 A_{ul}} \frac{J_\nu(T_{\text{ex}})}{[J_\nu(T_{\text{ex}}) - J_\nu(T_{\text{cmb}})]} \cdot \int T_{mb} d\nu \quad (\text{A.1})$$

where the integrated intensity is in  $\text{K km s}^{-1}$ , and the Einstein coefficient  $A_{ul}$  is in  $\text{s}^{-1}$  and with:

$$J_\nu(T) = \frac{h\nu/k}{\exp[h\nu/kT] - 1} \quad (\text{A.2})$$

where  $\nu$  is the frequency of the observed transition (e.g., Mangum & Shirley 2015). Then the total column density (which we will refer from now on as column density) can be calculated:

$$N_{\text{tot}} = N_u \cdot \frac{Q}{g_u \exp[-E_u/kT_{\text{ex}}]} \quad (\text{A.3})$$

In the cases where we could derive the optical depth  $\tau$  due to hyperfine splitting we corrected the column density using:

$$N_{\text{corr}} = N_{\text{tot}} \cdot \frac{\tau}{1 - \exp[-\tau]} \quad (\text{A.4})$$

In order to obtain abundances we derived  $\text{H}_2$  column densities either from dust maps obtained with Mambo with the IRAM 30m telescope at 1.2 mm (Beuther et al. 2002b) and a resolution of  $11''$ , or the galactic plane survey ATLASGAL (Schuller et al. 2009) at  $870\mu\text{m}$  and a resolution of  $19.2''$ , or the SCUBA Legacy Catalog (Di Francesco et al. 2008) at  $850\mu\text{m}$  and a resolution of  $22.9''$  (see Table A.1). The continuum data were smoothed to  $29''$  resolution in order to be beam matched with the IRAM 30m observations at 3 mm and the SMT molecular line data.  $\text{H}_2$  column densities were calculated from the observed peak intensities assuming optically thin emission and LTE following Equation A.5 (Schuller et al. 2009). The dust opacities used were  $\kappa_{850\mu\text{m}} = 1.48$ ,  $\kappa_{870\mu\text{m}} = 1.42$ ,  $\kappa_{1.2\text{mm}} = 0.97$ , interpolated values from Ossenkopf & Henning (1994), assuming grains with thin ice mantles, gas densities of  $n = 10^5 \text{ cm}^{-3}$ , and a gas-to-dust mass ratio  $R = 100$ . With these assumptions the  $\text{H}_2$  column density is calculated as:

$$N_{\text{H}_2} = \frac{F_\nu \cdot R}{B_\nu \cdot \Omega \cdot \kappa_\nu \cdot \mu \cdot m_H} \quad (\text{A.5})$$

The uncertainties in the derived  $\text{H}_2$  column densities are based largely on the dust and temperature properties and are approximately about a factor of 3. A more detailed description of the derivation is given in Gerner et al. (2014).

The molecular column densities are then divided by the  $\text{H}_2$  column densities and the averaged abundances are derived.

**Table A.1.** Source list showing the position, the distance, and the evolutionary stage of all high-mass star-forming regions.

source	$\alpha$ (J2000.0)	$\delta$ (J2000.0)	galactic $l$ [°]	galactic $b$ [°]	distance <sup>a</sup> [kpc]	type	24 $\mu$ m	70 $\mu$ m	continuum data <sup>b</sup>
IRDC011.1	18:10:28.4	-19:22:34	11.108	-0.115	3.6	IRDC	y	y	ATLASGAL
IRDC028.1	18:42:50.3	-04:03:20	28.343	0.060	4.8	IRDC	y	y	ATLASGAL
IRDC028.2	18:42:52.1	-03:59:54	28.397	0.080	4.8	IRDC	y	y	ATLASGAL
IRDC048.6	19:21:44.4	+13:49:24	48.657	-0.285	2.5	IRDC	n	n	ATLASGAL
IRDC079.1	20:32:22.0	+40:20:10	79.338	0.341	1.0	IRDC	-	y	SCUBA
IRDC079.3	20:31:57.7	+40:18:26	79.269	0.386	1.0	IRDC	-	y	SCUBA
IRDC18151	18:17:50.3	-12:07:54	18.319	1.792	3.0	IRDC	-	y	Mambo
IRDC18182	18:21:15.0	-14:33:03	16.578	-0.081	3.6	IRDC	y	y	Mambo
IRDC18223	18:25:08.3	-12:45:27	18.605	-0.075	3.7	IRDC	y	y	Mambo
IRDC18306	18:33:32.1	-08:32:28	23.297	0.0550	3.8	IRDC	n	n	Mambo
IRDC18308	18:33:34.3	-08:38:42	23.209	-0.001	4.9	IRDC	y	y	Mambo
IRDC18310	18:33:39.5	-08:21:10	23.478	0.115	5.2	IRDC	n	n	Mambo
IRDC18337	18:36:18.2	-07:41:00	24.374	-0.158	4.0	IRDC	y	y	Mambo
IRDC18385	18:41:17.4	-05:09:56	27.179	-0.104	3.3	IRDC	y	y <sup>c</sup>	Mambo
IRDC18437	18:46:21.8	-02:12:21	30.390	0.123	(6.2) 7.3 <sup>d</sup>	IRDC	y	y	Mambo
IRDC18454.1	18:48:02.1	-01:53:56	30.854	-0.109	(3.5) 6.4 <sup>e</sup>	IRDC	n	n	Mambo
IRDC18454.3	18:47:55.8	-01:53:34	30.848	-0.083	6.0 (6.4) <sup>f</sup>	IRDC	n	n	Mambo
IRDC19175	19:19:50.7	+14:01:23	48.617	0.214	1.1	IRDC	n	n	Mambo
IRDC20081	20:10:13.0	+27:28:18	66.145	-3.197	0.7	IRDC	-	n <sup>g</sup>	Mambo
HMPO18089	18:11:51.6	-17:31:29	12.889	0.489	3.6	HMPO			Mambo
HMPO18102	18:13:11.3	-18:00:03	12.623	-0.017	2.7	HMPO			Mambo
HMPO18151	18:17:58.1	-12:07:26	18.341	1.768	3.0	HMPO			Mambo
HMPO18182	18:21:09.2	-14:31:50	16.585	-0.051	3.9 <sup>h</sup>	HMPO			Mambo
HMPO18247	18:27:31.7	-11:45:56	19.755	-0.129	6.7	HMPO			Mambo
HMPO18264	18:29:14.6	-11:50:22	19.884	-0.535	3.28 <sup>h</sup>	HMPO			Mambo
HMPO18310	18:33:48.1	-08:23:50	23.455	0.063	5.2 (10.4) <sup>i</sup>	HMPO			Mambo
HMPO18488	18:51:25.6	+00:04:07	32.991	0.034	5.4 (8.9) <sup>j</sup>	HMPO			Mambo
HMPO18517	18:54:14.4	+04:41:40	37.430	1.517	2.9	HMPO			Mambo
HMPO18566	18:59:10.1	+04:12:14	37.554	0.200	6.7	HMPO			Mambo
HMPO19217	19:23:58.8	+16:57:44	51.679	0.720	10.5	HMPO			Mambo
HMPO19410	19:43:11.0	+23:44:10	59.784	0.066	2.1	HMPO			Mambo
HMPO20126	20:14:26.0	+41:13:32	78.122	3.633	1.7	HMPO			Mambo
HMPO20216	20:23:23.8	+41:17:40	79.127	2.279	1.7	HMPO			Mambo
HMPO20293	20:31:12.9	+40:03:20	78.982	0.352	1.3 (2.0) <sup>j</sup>	HMPO			Mambo
HMPO22134	22:15:09.1	+58:49:09	103.876	1.856	2.6	HMPO			Mambo
HMPO23033	23:05:25.7	+60:08:08	110.093	-0.067	3.5	HMPO			Mambo
HMPO23139	23:16:10.5	+59:55:28	111.256	-0.770	4.8	HMPO			Mambo
HMPO23151	23:17:21.0	+59:28:49	111.236	-1.238	5.7	HMPO			Mambo
HMPO23545	23:57:06.1	+65:24:48	117.315	3.136	0.8	HMPO			Mambo
HMC009.62	18:06:15.2	-20:31:37	9.621	0.193	5.7	HMC			ATLASGAL
HMC010.47	18:08:38.2	-19:51:50	10.472	0.027	5.8	HMC			ATLASGAL
HMC029.96	18:46:04.0	-02:39:21	29.956	-0.017	7.4	HMC			ATLASGAL
HMC031.41	18:47:34.2	-01:12:45	31.412	0.308	7.9	HMC			ATLASGAL
HMC034.26	18:53:18.5	+01:14:58	34.257	0.154	4.0	HMC			ATLASGAL
HMC045.47	19:14:25.7	+11:09:26	45.466	0.045	6.0	HMC			ATLASGAL
HMC075.78	20:21:44.1	+37:26:40	75.783	0.343	4.1	HMC			SCUBA
NGC7538B	23:13:45.4	+61:28:11	111.542	0.777	2.65 (5.61) <sup>j</sup>	HMC			SCUBA
Orion-KL	05:35:14.4	-05:22:31	208.993	-19.385	0.44	HMC			SCUBA
W3IRS5	02:25:40.7	+62:05:52	133.715	1.215	1.8	HMC			SCUBA
W3H <sub>2</sub> O	02:27:04.6	+61:52:25	133.949	1.065	2.0	HMC			SCUBA
UCH005.89	18:00:30.4	-24:04:00	5.886	-0.392	2.5	UCHII			ATLASGAL
UCH010.10	18:05:13.1	-19:50:35	10.099	0.739	4.4	UCHII			ATLASGAL
UCH010.30	18:08:55.8	-20:05:55	10.300	-0.147	6.0	UCHII			ATLASGAL
UCH012.21	18:12:39.7	-18:24:20	12.208	-0.102	13.5	UCHII			ATLASGAL
UCH013.87	18:14:35.8	-16:45:43	13.872	0.280	4.4	UCHII			ATLASGAL
UCH030.54	18:46:59.3	-02:07:24	30.535	0.021	6.1	UCHII			ATLASGAL
UCH035.20	19:01:46.4	+01:13:25	35.200	-1.741	3.2	UCHII			SCUBA
UCH045.12	19:13:27.8	+10:53:37	45.122	0.132	6.9	UCHII			ATLASGAL
UCH045.45	19:14:21.3	+11:09:14	45.454	0.060	6.0	UCHII			ATLASGAL

**Notes.** For the IRDCs we indicate whether or not they show embedded 24 or 70  $\mu$ m point sources with y(es) or n(o) (or “-” if there are no data available). In the last column the sources of the dust continuum data are presented.

<sup>(a)</sup> Unbracketed values are preferred, bracketed values are alternative values <sup>(b)</sup> Dust continuum data. Either from IRAM 30m observations with Mambo (1.2mm), the galactic plane survey ATLASGAL (870  $\mu$ m) (Schuller et al. 2009) or the SCUBA Legacy Catalog (850  $\mu$ m) (Di Francesco et al. 2008). <sup>(c)</sup> Very weak emission compared with the background located at the same position as 24  $\mu$ m emission source <sup>(d)</sup> For  $v_{\text{lsr}} = (97.6)111.3 \text{ km s}^{-1}$  <sup>(e)</sup> For  $v_{\text{lsr}} = (52.8)100.2 \text{ km s}^{-1}$  <sup>(f)</sup> For  $v_{\text{lsr}} = 94.3(98.4) \text{ km s}^{-1}$  <sup>(g)</sup> No embedded central point source found, a nearby extended source with emission inside the beam is detected <sup>(h)</sup> Ellsworth-Bowers et al. subm. <sup>(i)</sup> For the near (far) kinematic solution <sup>(j)</sup> Parallaxial (kinematic) distance

**Table A.2.** Luminosity, H<sub>2</sub>, DCO<sup>+</sup>, DCN, DNC and N<sub>2</sub>D<sup>+</sup> column density and the corresponding error ( $\Delta$ ) for each source. The errors show the uncertainties in the measured integrated flux.

Source	Luminosity log L <sub>Sun</sub>	H <sub>2</sub> cm <sup>-2</sup>	DCO <sup>+</sup> cm <sup>-2</sup>	$\Delta$ (DCO <sup>+</sup> ) cm <sup>-2</sup>	DCN cm <sup>-2</sup>	$\Delta$ (DCN) cm <sup>-2</sup>	DNC	$\Delta$ (DNC)	N <sub>2</sub> D <sup>+</sup>	$\Delta$ (N <sub>2</sub> D <sup>+</sup> )
IRDC011.1	3.16 <sup>a</sup>	3.7(22)	4.5(11)	1.2(11)	$\leq 4.1(11)$	3.7(11)	9.3(11)	1.4(11)	$\leq 3.9(11)$	9.6(10)
IRDC028.1		3.2(22)	$\leq 1.9(11)$	4.8(10)	$\leq 5.4(11)$	1.1(11)	$\leq 4.3(11)$	9.7(10)	$\leq 6.8(11)$	9.6(10)
IRDC028.2	3.47 <sup>a</sup>	1.1(23)	9.3(11)	1.1(11)	3.4(12)	3.2(11)	1.5(12)	2(11)	$\leq 6.6(11)$	1.9(11)
IRDC048.6	0.78 <sup>a</sup>	8.6(21)	1.2(12)	7.1(10)	$\leq 9(11)$	1.9(11)	$\leq 4.7(11)$	2(11)	$\leq 9.6(11)$	2.5(11)
IRDC079.1	2.05 <sup>a</sup>	4.3(22)	3.9(12)	8.9(10)	$\leq 8.1(11)$	5.1(11)	2.7(12)	1.5(11)	1.5(12)	2.4(11)
IRDC079.3	1.4 <sup>a</sup>	2.7(22)	3(12)	1(11)	$\leq 9.6(11)$	6.9(11)	1.9(12)	1.5(11)	2.1(12)	3.3(11)
IRDC18151	2.66 <sup>a</sup>	5.1(22)	3(12)	1.3(11)	2.3(12)	2.8(11)	3.2(12)	2.3(11)	1.4(12)	2.1(11)
IRDC18182	2.13 <sup>a</sup>	1.3(22)	5.4(11)	8(10)	$\leq 5.4(11)$	4.3(11)	$\leq 5.7(11)$	1.2(11)	$\leq 5.5(11)$	8.2(10)
IRDC18223	2.51 <sup>a</sup>	2(22)	9.7(11)	1.4(11)	1.3(12)	3.4(11)	3.2(12)	2.5(11)	1.2(12)	1.8(11)
IRDC18306		1.7(22)	$\leq 3(11)$	9.8(10)	$\leq 5.7(11)$	2(11)	$\leq 6.3(11)$	1(11)	$\leq 5.5(11)$	2.1(11)
IRDC18308	2.12 <sup>a</sup>	2.4(22)	$\leq 2.8(11)$	9.3(10)	$\leq 6.1(11)$	1.5(11)	$\leq 5.3(11)$	2(11)	$\leq 6.8(11)$	3.6(11)
IRDC18310		1.6(22)	$\leq 2.9(11)$	1.9(11)	$\leq 6.8(11)$	2.9(11)	$\leq 4.5(11)$	3.1(11)	$\leq 6.8(11)$	3.6(11)
IRDC18337	2.25 <sup>a</sup>	7.8(21)	$\leq 2.8(11)$	1(11)	$\leq 5(11)$	2.9(11)	$\leq 3.9(11)$	2.2(11)	$\leq 5.8(11)$	1.5(11)
IRDC18385	1.23 <sup>a</sup>	7.7(21)	$\leq 3.1(11)$	9.8(10)	$\leq 6.1(11)$	1.2(11)	$\leq 5.9(11)$	2.2(11)	$\leq 5.7(11)$	1(11)
IRDC18437	2.23 <sup>a</sup>	1(22)	$\leq 3.1(11)$	1.4(11)	$\leq 5.9(11)$	1.2(11)	$\leq 5.3(11)$	1.6(11)	$\leq 5(11)$	3.7(11)
IRDC18454.1	3.6 <sup>b</sup>	1.4(22)	$\leq 2.9(11)$	1.1(11)	$\leq 5.2(11)$	1.5(11)	$\leq 6.1(11)$	1.3(11)		6.9(11)
IRDC18454.3	2.37 <sup>a</sup>	2(22)	$\leq 3.1(11)$	7.3(10)	$\leq 5.5(11)$	2.5(11)	$\leq 7.3(11)$	1.7(11)		5.9(11)
IRDC19175	-1 <sup>a</sup>	9.1(21)	$\leq 2.7(11)$	9.2(10)	$\leq 5.4(11)$	2.8(11)	$\leq 4.5(11)$	1.3(11)	$\leq 6.5(11)$	1.6(11)
IRDC20081		2(22)	1.4(12)	7.4(10)	$\leq 6.1(11)$	4(11)	9.1(11)	1.3(11)	8.1(11)	1.3(11)
HMPO18089	4.5 <sup>c</sup>	8.2(22)	1.7(12)	9(10)	6.8(12)	2.5(11)	9.7(11)	1.3(11)	$\leq 4.2(11)$	9.1(10)
HMPO18102	2.92 <sup>c</sup>	4.2(22)	$\leq 1.2(11)$	9.7(10)	$\leq 3.8(11)$	2.6(11)	1.1(12)	1.2(11)	$\leq 3.8(11)$	2.1(11)
HMPO18151	2.03 <sup>c</sup>	4.3(22)	8.1(11)	4.4(10)	3.2(12)	1.3(11)	2.1(12)	9.5(10)	3.4(11)	7.6(10)
HMPO18182	3.77 <sup>c</sup>	5.5(22)	9.5(11)	7.8(10)	3(12)	2.1(11)	1.7(12)	1.6(11)	$\leq 3.7(11)$	6.4(10)
HMPO18247	4.8 <sup>c</sup>	2.8(22)	$\leq 1.3(11)$	2.2(10)	$\leq 3.7(11)$	1.8(11)	$\leq 2(11)$	1.2(11)	$\leq 4.1(11)$	6.6(10)
HMPO18264	4 <sup>c</sup>	9.4(22)	2.4(12)	6.4(10)	6.9(12)	1.6(11)	4.4(12)	1.1(11)	1(12)	1.5(11)
HMPO18310	3.48 <sup>c</sup>	2.9(22)	$\leq 1.6(11)$	1(11)	$\leq 4.1(11)$	3.3(11)	$\leq 3.1(11)$	1.5(11)	6.7(11)	1.3(11)
HMPO18488	4.5 <sup>c</sup>	3.2(22)	2.4(11)	5.2(10)	1.4(12)	1.8(11)	$\leq 2.1(11)$	9.4(10)	$\leq 3.3(11)$	1.2(11)
HMPO18517	4.1 <sup>c</sup>	7(22)	2(12)	5.6(10)	5.6(12)	2.3(11)	1.6(12)	1.3(11)	$\leq 3.9(11)$	1.2(11)
HMPO18566	4.8 <sup>c</sup>	2.5(22)	3.8(11)	1.4(11)	2.3(12)	2.4(11)	8.1(11)	1.3(11)	$\leq 4.1(11)$	1.6(07)
HMPO19217	4.9 <sup>c</sup>	4.2(22)	6.4(11)	9.6(10)	2.6(12)	2.3(11)	$\leq 2.9(11)$	2.4(11)	$\leq 3(11)$	7.6(10)
HMPO19410	4 <sup>c</sup>	6.8(22)	1.3(12)	6.2(10)	3.5(12)	1.5(11)	2.6(12)	1.1(11)	1.5(12)	1.1(11)
HMPO20126	3.9 <sup>c</sup>	5.7(22)	1.3(12)	8(10)	7.4(12)	1.8(11)	3.6(12)	1.3(11)	7.7(11)	1.2(11)
HMPO20216	3.3 <sup>c</sup>	1.3(22)	4.9(11)	6.4(10)	1.1(12)	1.4(11)	1.2(12)	9.8(10)	$\leq 3(11)$	1.4(11)
HMPO20293	3.4 <sup>c</sup>	4.3(22)	9.9(11)	7(10)	1.9(12)	2.4(11)	1.6(12)	1(11)	1.7(12)	1.6(11)
HMPO22134	4.1 <sup>c</sup>	2.4(22)	6.9(11)	5.3(10)	1.2(12)	1.4(11)	3.6(11)	6.3(10)	$\leq 2.8(11)$	1.6(11)
HMPO23033	4 <sup>c</sup>	4(22)	1.2(12)	7.9(10)	2.1(12)	2.6(11)	1.1(12)	1.6(11)	3.9(11)	1(11)
HMPO23139	4.4 <sup>c</sup>	3(22)	2.8(11)	7.9(10)	1.7(12)	1.5(11)	$\leq 2.5(11)$	5.6(10)	$\leq 2.3(11)$	1.6(11)
HMPO23151	5 <sup>c</sup>	2.3(22)	$\leq 1.2(11)$	5.4(10)	6.1(11)	1.1(11)	$\leq 2.3(11)$	9(10)	$\leq 2.5(11)$	1.6(11)
HMPO23545	3 <sup>c</sup>	1.5(22)	1.5(11)	5.2(10)	$\leq 3.3(11)$	1.6(11)	$\leq 2.7(11)$	9(10)	$\leq 3.1(11)$	1.7(11)
HMC009.62	4.3 <sup>d</sup>	9.5(22)	8.7(11)	9.6(10)	5.6(12)	1.1(11)	6.1(11)	7.6(10)	$\leq 1.7(11)$	1.4(11)
HMC010.47	5.5 <sup>e</sup>	2.3(23)	6(12)	7(10)	1.2(13)	2.9(11)		3(11)		5.4(11)
HMC029.96	6 <sup>e</sup>	9.4(22)	3.6(11)	1.2(11)	6.4(12)	1.7(11)	8.7(11)	8.6(10)	$\leq 3.1(11)$	1.4(11)
HMC031.41	5.2 <sup>e</sup>	1.6(23)	5(12)	7.8(10)	8(12)	1.4(11)	5.8(11)	1.3(11)		1.8(11)
HMC034.26	5.7 <sup>e</sup>	4.1(23)	5.9(12)	8.7(10)	1.9(13)	1.7(11)	2.5(12)	1.5(11)	$\leq 3.3(11)$	1.7(11)
HMC045.47	5.6 <sup>e</sup>	4.5(22)	2.8(11)	5.5(10)	1.7(12)	1.3(11)	7.3(11)	1.3(11)	$\leq 2.5(11)$	2(11)
HMC075.78	5.3 <sup>e</sup>	6.3(22)	1.1(12)	5.5(10)	4.9(12)	1.3(11)	1.1(12)	7.7(10)	$\leq 1.9(11)$	1.2(11)
W3H2O	4.48 <sup>f</sup>	7.4(22)	3.4(12)	9.1(10)	1.6(13)	1.5(11)	2.1(12)	7.8(10)	$\leq 2.8(11)$	5.8(10)
W3IRS5	5.3 <sup>g</sup>	6(22)	4.2(11)	7.6(10)	1.5(12)	1.1(11)	$\leq 1.8(11)$	1.2(11)	$\leq 1.7(11)$	7.1(10)
NGC7538B	5.8 <sup>e</sup>	1.2(23)	2(12)	7.8(10)	1.4(13)	1.5(11)	1.5(12)	1(11)	$\leq 1.6(11)$	7.1(10)
Orion-KL	5 <sup>h</sup>	1.3(24)	2.8(13)	1.6(11)	1.3(14)	1.6(12)		4.3(11)		1.2(12)
UCH005.89	5.3 <sup>e</sup>	2.2(23)	1.3(12)	1.6(11)	2.1(13)	1.5(11)	6.3(12)	2.3(11)	$\leq 2.5(11)$	5.8(10)
UCH010.10		6.4(21)	$\leq 1.9(11)$	2.2(10)	$\leq 2.8(11)$	1.5(11)	$\leq 3(11)$	1.8(11)	$\leq 2.8(11)$	6.9(10)
UCH010.30	5.8 <sup>e</sup>	8.1(22)	7(11)	1.1(11)	3.7(12)	2.1(11)	1.9(12)	1.4(11)	$\leq 3.5(11)$	1.2(11)
UCH012.21	5.8 <sup>e</sup>	9.6(22)	$\leq 2.1(11)$	2.5(10)	5.2(12)	2.6(11)	$\leq 2.3(11)$	1.3(11)	$\leq 4.1(11)$	1.6(11)
UCH013.87	5.2 <sup>e</sup>	5.3(22)	4.7(11)	6.4(10)	1.7(12)	1.6(11)	$\leq 3(11)$	5.5(10)	$\leq 3.3(11)$	3.2(11)
UCH030.54	5.7 <sup>i</sup>	2.1(22)	2.4(11)	8.3(10)	$\leq 3.2(11)$	2.2(11)	$\leq 2.3(11)$	1.1(11)	$\leq 3.4(11)$	1.8(11)
UCH035.20	5.3 <sup>e</sup>	1.1(23)	5.6(11)	1(11)	3.6(12)	1.9(11)	1.4(12)	2(11)	$\leq 3.1(11)$	1.3(11)
UCH045.12	5.9 <sup>e</sup>	7.4(22)	4.6(11)	8.5(10)	1.8(12)	2.1(11)	6.1(11)	1.3(11)	$\leq 2.7(11)$	1.9(11)
UCH045.45	5.7 <sup>e</sup>	4.2(22)	$\leq 1.2(11)$	1(11)	1.9(12)	2.2(11)	$\leq 1.9(11)$	1.8(11)	$\leq 3.5(11)$	1.9(11)

**Notes.** Column densities written as  $a(x) = a \times 10^x$ . H<sub>2</sub> column density is averaged over a 29''-beam and for all other molecules over a 30''-beam.<sup>(a)</sup> Ragan et al. (2012) <sup>(b)</sup> Beuther et al. (2012) <sup>(c)</sup> Sridharan et al. (2002) <sup>(d)</sup> Linz et al. (2005) <sup>(e)</sup> Churchwell et al. (1990) <sup>(f)</sup> Chen et al. (2006) <sup>(g)</sup> Campbell et al. (1995) <sup>(h)</sup> Beuther et al. (2004) <sup>(i)</sup> Wood & Churchwell (1989a)

**Table A.3.** HCO<sup>+</sup>, HCN, HNC and N<sub>2</sub>H<sup>+</sup> column density and corresponding error ( $\Delta$ ) for each source. The errors show the uncertainties in the measured integrated fluxes and determined optical depths.

Source	HCO <sup>+</sup> cm <sup>-2</sup>	$\Delta$ (HCO <sup>+</sup> ) cm <sup>-2</sup>	HCN cm <sup>-2</sup>	$\Delta$ (HCN) cm <sup>-2</sup>	HNC	$\Delta$ (HNC)	N <sub>2</sub> H <sup>+</sup>	$\Delta$ (N <sub>2</sub> H <sup>+</sup> )
IRDC011.1	1.5(14)	2.0(12)	6.7(13)	4.2(12)	2.1(14)	4.2(12)	2.8(13)	9.5(11)
IRDC028.1	1.4(14)	2.3(12)	1.2(14)	4.9(12)	2.2(14)	4.8(12)	4.0(13)	3.2(11)
IRDC028.2	1.8(14)	2.3(12)	1.9(14)	8.0(12)	2.2(14)	4.8(12)	6.5(13)	2.5(12)
IRDC048.6	7.9(13)	2.4(12)	2.7(13)	3.0(13)	6.1(14)	5.0(12)	8.0(12)	8.4(11)
IRDC079.1	2.3(14)	4.1(12)	7.2(13)	2.4(12)	1.5(14)	8.5(12)	2.3(13)	1.8(12)
IRDC079.3	2.1(14)	4.0(12)	7.2(13)	7.1(13)	2.3(14)	8.2(12)	2.5(13)	2.2(12)
IRDC18151	2.3(14)	2.2(12)	1.6(14)	2.8(14)	1.8(14)	4.5(12)	4.9(13)	1(12)
IRDC18182	6.9(13)	2.1(12)	3.4(13)	2.4(12)	9.7(13)	4.3(12)	1.6(13)	5.8(11)
IRDC18223	2.1(14)	2.0(12)	1.2(14)	1.4(14)	3.6(14)	4.2(12)	3.7(13)	2.2(11)
IRDC18306	5.2(13)	2.0(12)			9.4(13)	4.1(12)	1.6(13)	1.8(12)
IRDC18308	6.1(13)	1.6(12)	2.0(14)	1.1(14)	9.0(13)	3.3(12)	2.2(13)	3.9(10)
IRDC18310	7.1(13)	1.7(12)	6.6(13)	3.4(12)	1.6(14)	3.5(12)	3.3(13)	6.9(11)
IRDC18337	6.9(13)	1.2(12)	6.9(13)	3.0(12)	8.3(13)	2.4(12)	1.8(13)	3.6(11)
IRDC18385	3.9(13)	2.8(12)	2.0(13)	7.2(13)	4.7(13)	5.8(12)	1.1(13)	1.8(13)
IRDC18437	5.2(13)	2.1(12)	2.0(13)	3.0(12)	6.0(13)	4.4(12)	1.5(13)	1.5(12)
IRDC18454.1	4.5(13)	2.2(12)			6.6(13)	4.6(12)	1.9(13)	2.2(12)
IRDC18454.3	1.8(14)	2.2(12)	1.3(14)	5.0(12)	2.0(14)	4.6(12)	3.2(13)	7.9(11)
IRDC19175	5.4(13)	3.2(12)	1.8(13)	1.6(12)	5.2(13)	6.6(12)	5.6(12)	2.3(12)
IRDC20081	1.2(14)	3.9(12)	1.2(14)	1.1(14)	5.6(13)	8.1(12)	6.5(12)	1.5(12)
HMPO18089	5.0(14)	2.6(12)	2.0(14)	1.5(12)	5.5(14)	5.4(12)	4.9(13)	3.7(11)
HMPO18102	3.5(14)	3.0(12)	1.8(14)	1.7(12)	5.0(14)	6.2(12)	6.5(13)	1.2(12)
HMPO18151	4.0(14)	2.7(12)	1.8(14)	1.6(12)	2.8(14)	5.6(12)	3.6(13)	4.1(12)
HMPO18182	3.8(14)	2.4(12)	1.3(14)	7.0(14)	3.1(14)	5.1(12)	6.4(13)	2.4(11)
HMPO18247	9.4(13)	1.7(12)	1.2(14)	8.0(13)	1.1(14)	3.6(12)	3.7(13)	4.4(12)
HMPO18264	5.4(14)	2.7(12)	8.6(14)	4.1(14)	3.4(14)	5.6(12)	1.1(14)	3.1(12)
HMPO18310	1.9(14)	2.1(12)	5.9(13)	1.2(12)	2.0(14)	4.3(12)	3.1(13)	1.5(11)
HMPO18488	2.5(14)	3.1(12)	1.3(14)	1.4(12)	2.0(14)	6.3(12)	4.1(13)	1.5(13)
HMPO18517	6.2(14)	3.7(12)	1.8(14)	8.2(11)	2.7(14)	7.7(12)	7.6(13)	9.6(12)
HMPO18566	3.3(14)	3.1(12)	1.3(14)	1.5(12)	3.3(14)	6.4(12)	5.5(13)	1.2(12)
HMPO19217	5.2(14)	4.4(12)	8.3(13)	1.8(12)	3.2(14)	9.1(12)	4.7(13)	5.2(11)
HMPO19410	4.4(14)	3.7(12)	1.4(14)	7.5(11)	4.1(14)	7.7(12)	1.0(14)	1.3(12)
HMPO20126	5.9(14)	7.0(12)	1.9(14)	1.2(15)	6.6(14)	1.4(13)	7.6(13)	6.4(11)
HMPO20216	2.0(14)	6.2(12)	5.9(13)	1.4(12)	1.5(14)	1.3(13)	1.0(13)	3.0(12)
HMPO20293	3.9(14)	5.0(12)	1.1(14)	3.7(14)	4.2(14)	1.0(13)	1.1(14)	3.7(12)
HMPO22134	1.9(14)	3.8(12)	1.2(14)	4.7(13)	7.9(13)	7.9(12)	1.1(13)	4.0(11)
HMPO23033	6.2(14)	4.1(12)	1.8(14)	1.9(13)	3.0(14)	8.5(12)	4.5(13)	1.2(12)
HMPO23139	3.0(14)	4.2(12)	3.0(14)	1.4(14)	1.5(14)	8.8(12)	3.0(13)	1.3(12)
HMPO23151	1.1(14)	4.7(12)	5.4(13)	4(13)	6.0(13)	9.7(12)	1.1(12)	8.0(12)
HMPO23545	1.3(14)	3.8(12)	2.4(13)	5(12)	4.1(13)	7.8(12)	2.3(12)	1.2(12)
HMC009.62	7.6(14)	2.2(12)	3.2(14)	1.1(13)	5.5(14)	4.5(12)	1.0(14)	3.8(11)
HMC010.47	8.7(14)	2.3(12)	3.5(14)	1.9(12)	8.1(14)	4.8(12)	1.6(14)	3.9(12)
HMC029.96	7.1(14)	2.7(12)	4.2(14)	1.8(12)	5.5(14)	5.6(12)	5.9(13)	5.6(11)
HMC031.41	3.4(14)	2.9(12)	1.0(14)	3.9(12)	4.9(14)	6.1(12)	4.4(13)	2.3(12)
HMC034.26	2.1(15)	3.8(12)	5.0(14)	1.4(13)	1.6(15)	8.0(12)	9.7(13)	1.5(12)
HMC045.47	9.0(14)	3.6(12)	1.2(14)	1(12)	6.4(14)	7.5(12)	7.3(13)	6.4(11)
HMC075.78	9.3(14)	6.7(12)	1.8(14)	1.3(12)	4.6(14)	1.4(13)	5.5(13)	9.5(11)
W3H2O	8.9(14)	5.5(12)	5.5(14)	5.6(14)	3.3(14)	1.1(13)	2.0(13)	2.0(12)
W3IRS5	3.6(14)	3.4(12)	3.3(14)	1.6(12)	1.3(14)	7(12)	2.2(12)	4.4(11)
NGC7538B	7.2(14)	5.1(12)	4.5(14)	3.1(12)	3.0(14)	1.1(13)	1.3(13)	1.0(12)
Orion-KL	7.3(14)	1(13)	1.2(16)	3.1(13)	7.3(14)	2.1(13)	4.3(12)	1.5(12)
UCH005.89	2.1(15)	4.1(12)	1.3(15)	5.3(12)	2.6(15)	8.5(12)	2.1(14)	7.2(11)
UCH010.10	5.5(13)	1.9(12)	3.6(13)	2.8(13)	1.1(14)	4(12)	2.1(13)	7.3(13)
UCH010.30	4.9(14)	1.9(12)	6.7(14)	2.9(12)	4.9(14)	4(12)	1.3(14)	6.0(11)
UCH012.21	5.9(14)	3.2(12)	2.6(14)	3.7(12)	5.9(14)	6.6(12)	7.3(13)	3.1(13)
UCH013.87	3.8(14)	2.6(12)	4.1(14)	2.5(12)	2.0(14)	5.4(12)	3.9(13)	3.3(11)
UCH030.54	1.1(14)	2.7(12)	1.0(14)	8.5(11)	5.4(13)	5.5(12)	5.8(12)	2.0(12)
UCH035.20	3.6(14)	3.4(12)	3.4(14)	1.3(12)	2.5(14)	6.9(12)	3.7(13)	3.4(11)
UCH045.12	4.2(14)	3.5(12)	5.6(14)	2.5(12)	1.7(14)	7.2(12)	8.7(12)	1.7(12)
UCH045.45	1.9(14)	3.3(12)	1.4(14)	1.1(12)	1.3(14)	6.8(12)	2.1(13)	4.3(11)

**Notes.** Column densities written as  $a(x) = a \times 10^x$ . H<sub>2</sub> column density is averaged over a 29''-beam and for all other molecules over a 30''-beam. The given errors are uncertainties in the measured integrated fluxes and the optical depth  $\tau$ . The high uncertainties in some cases are due to high uncertainties in the determined optical depth.

**Table A.4.** Parameters of the best-fit IRDC model.

Parameter	Symbol	Model
Inner radius	$r_0$	12 700 AU
Outer radius	$r_1$	0.5 pc <sup>a</sup>
Density at the inner radius	$\rho_0$	$1.4 \times 10^5 \text{ cm}^{-3}$
Average density with a beam of 26 000 AU	$\bar{\rho}$	$8.9 \times 10^4 \text{ cm}^{-3}$
Average density with a beam of 54 000 AU	$\bar{\rho}$	$5.2 \times 10^4 \text{ cm}^{-3}$
Density profile	$p$	1.5
Temperature at the inner radius	$T_0$	11.3 K
Average temperature	$\bar{T}$	11.3 K
Temperature profile	$q$	0
Lifetime		16 500 years

**Notes.**

<sup>(a)</sup> This value is limited by the largest 29'' IRAM beam size used in our observations.

**Table A.5.** Parameters of the best-fit HMPO model.

Parameter	Symbol	Model
Inner radius	$r_0$	103 AU
Outer radius	$r_1$	0.5 pc <sup>a</sup>
Density at the inner radius	$\rho_0$	$1.5 \times 10^9 \text{ cm}^{-3}$
Average density with a beam of 21 700 AU	$\bar{\rho}$	$1.6 \times 10^6 \text{ cm}^{-3}$
Average density with a beam of 57 300 AU	$\bar{\rho}$	$3.7 \times 10^5 \text{ cm}^{-3}$
Density profile	$p$	1.8
Temperature at the inner radius	$T_0$	75.8 K
Average temperature	$\bar{T}$	21.5 K
Temperature profile	$q$	0.4
Lifetime		32 000 years

**Notes.**

<sup>(a)</sup> This value is limited by the largest 29'' IRAM beam size used in our observations.

**Table A.6.** Parameters of the best-fit HMC model.

Parameter	Symbol	Model
Inner radius	$r_0$	1 140 AU
Outer radius	$r_1$	0.5 pc <sup>a</sup>
Density at the inner radius	$\rho_0$	$1.3 \times 10^8 \text{ cm}^{-3}$
Average density with a beam of 45 400 AU	$\bar{\rho}$	$1.7 \times 10^6 \text{ cm}^{-3}$
Average density with a beam of 63 100 AU	$\bar{\rho}$	$9.6 \times 10^5 \text{ cm}^{-3}$
Density profile	$p$	2.0
Temperature at the inner radius	$T_0$	162.9 K
Average temperature	$\bar{T}$	50 – 55 K
Temperature profile	$q$	0.4
Lifetime		35 000 years

**Notes.**

<sup>(a)</sup> This value is limited by the largest 29'' IRAM beam size used in our observations.

**Table A.7.** Parameters of the best-fit UCHII model.

Parameter	Symbol	Model
Inner radius	$r_0$	103 AU
Outer radius	$r_1$	0.5 pc <sup>a</sup>
Density at the inner radius	$\rho_0$	$1.0 \times 10^{10} \text{ cm}^{-3}$
Average density with a beam of 57 800 AU	$\bar{\rho}$	$1.3 \times 10^6 \text{ cm}^{-3}$
Average density with a beam of 85 400 AU	$\bar{\rho}$	$7.1 \times 10^5 \text{ cm}^{-3}$
Density profile	$p$	2.0
Temperature at the inner radius	$T_0$	244.3 K
Average temperature	$\bar{T}$	31 – 34 K
Temperature profile	$q$	0.4
Lifetime		3 000 years

**Notes.**

<sup>(a)</sup> This value is limited by the largest 29'' IRAM beam size used in our observations.

**Table A.8.** Median column densities in  $a(x) = a \times 10^x$  for observations (including detections and upper limits) and best-fit IRDC model. Modeled best-fit values in italics do not agree with the observed values within one order of magnitude. If the molecule is detected in less than 50% of the sources we marked it as an upper limit.

Molecule	Obs. col. den. [cm <sup>-2</sup> ]	Mod. col. den. [cm <sup>-2</sup> ]
CO	1.9(18)	2.8(18)
HNC	9.7(13)	5.8(14)
HCN	7.2(13)	7.1(14)
HCO <sup>+</sup>	7.9(13)	8.9(13)
HNCO	2.4(12)	2.7(12)
H <sub>2</sub> CO	1.7(13)	5.1(13)
N <sub>2</sub> H <sup>+</sup>	2.2(13)	2.2(12)
CS	≤4.7(14)	6.8(14)
SO	≤6.6(12)	5.4(13)
OCS	≤4.2(14)	4.0(12)
C <sub>2</sub> H	4.8(14)	2.5(14)
SiO	2.3(12)	3.5(12)
CH <sub>3</sub> CN	≤3.7(12)	1.3(13)
CH <sub>3</sub> OH	≤4.1(13)	2.8(13)
DCO <sup>+</sup>	≤3.1(11)	5.9(11)
DCN	≤6.1(11)	2.4(12)
DNC	≤6.1(11)	1.6(11)
N <sub>2</sub> D <sup>+</sup>	≤6.8(11)	4.0(8)
Agreement		18/18 = 100%

**Table A.9.** Median column densities in  $a(x) = a \times 10^x$  for observations (including detections and upper limits) and best-fit HMPO model. Modeled best-fit values in italics do not agree with the observed values within one order of magnitude. If the molecule is detected in less than 50% of the sources we marked it as an upper limit.

Molecule	Obs. col. den. [cm <sup>-2</sup> ]	Mod. col. den. [cm <sup>-2</sup> ]
CO	5.0(18)	6.9(18)
HNC	2.9(14)	5.3(14)
HCN	1.3(14)	6.4(14)
HCO <sup>+</sup>	3.7(14)	3.6(14)
HNCO	3.8(12)	3.6(13)
H <sub>2</sub> CO	4.1(13)	3.8(13)
N <sub>2</sub> H <sup>+</sup>	4.6(13)	6.6(13)
CS	1.1(15)	3.9(14)
SO	8.2(13)	1.8(15)
OCS	≤2.0(14)	3.7(13)
C <sub>2</sub> H	1.9(15)	2.0(14)
SiO	5.9(12)	1.2(13)
CH <sub>3</sub> CN	3.4(12)	7.7(12)
CH <sub>3</sub> OH	1.4(14)	3.3(12)
DCO <sup>+</sup>	6.7(11)	3.9(12)
DCN	2.0(12)	3.0(12)
DNC	1.0(12)	2.0(12)
N <sub>2</sub> D <sup>+</sup>	≤3.8(11)	6.3(11)
Agreement		16/18 = 89%

**Table A.10.** Median column densities in  $a(x) = a \times 10^x$  for observations (including detections and upper limits) and best-fit HMC model. Modeled best-fit values in italics do not agree with the observed values within one order of magnitude. If the molecule is detected in less than 50% of the sources we marked it as an upper limit.

Molecule	Obs. col. den. [cm <sup>-2</sup> ]	Mod. col. den. [cm <sup>-2</sup> ]
CO	2.2(19)	6.8(19)
HNC	5.5(14)	1.7(15)
HCN	3.5(14)	2.0(15)
HCO <sup>+</sup>	7.6(14)	1.5(15)
HNCO	1.7(13)	5.0(16)
H <sub>2</sub> CO	2.7(14)	2.6(14)
N <sub>2</sub> H <sup>+</sup>	5.5(13)	7.8(13)
CS	1.3(16)	7.5(15)
SO	5.2(14)	6.6(16)
OCS	1.7(15)	1.3(15)
C <sub>2</sub> H	4.3(15)	2.4(14)
SiO	2.2(13)	5.6(13)
CH <sub>3</sub> CN	5.2(13)	6.0(13)
CH <sub>3</sub> OH	8.7(14)	3.2(12)
DCO <sup>+</sup>	2.0(12)	1.7(13)
DCN	8.0(12)	8.9(12)
DNC	8.7(11)	8.1(12)
N <sub>2</sub> D <sup>+</sup>	≤2.2(11)	5.5(11)
Agreement		14/18 = 78%

**Table A.11.** Median column densities in  $a(x) = a \times 10^x$  for observations (including detections and upper limits) and best-fit UCHn model. Modeled best-fit values in italics do not agree with the observed values within one order of magnitude. If the molecule is detected in less than 50% of the sources we marked it as an upper limit.

Molecule	Obs. col. den. [cm <sup>-2</sup> ]	Mod. col. den. [cm <sup>-2</sup> ]
CO	1.4(19)	3.7(19)
HNC	2.0(14)	2.2(14)
HCN	3.4(14)	2.7(14)
HCO <sup>+</sup>	3.8(14)	6.6(14)
HNCO	2.7(12)	3.9(15)
H <sub>2</sub> CO	7.5(13)	3.5(13)
N <sub>2</sub> H <sup>+</sup>	3.7(13)	4.9(13)
CS	2.3(15)	1.9(15)
SO	7.7(13)	3.5(16)
OCS	≤5.1(13)	2.9(14)
C <sub>2</sub> H	3.0(15)	6.0(13)
SiO	3.4(12)	3.7(13)
CH <sub>3</sub> CN	8.6(12)	1.1(13)
CH <sub>3</sub> OH	6.6(13)	5.6(13)
DCO <sup>+</sup>	4.6(11)	7.0(12)
DCN	1.9(12)	1.3(12)
DNC	≤3.0(11)	1.0(12)
N <sub>2</sub> D <sup>+</sup>	≤3.3(11)	3.9(11)
Agreement		13/18 = 72%



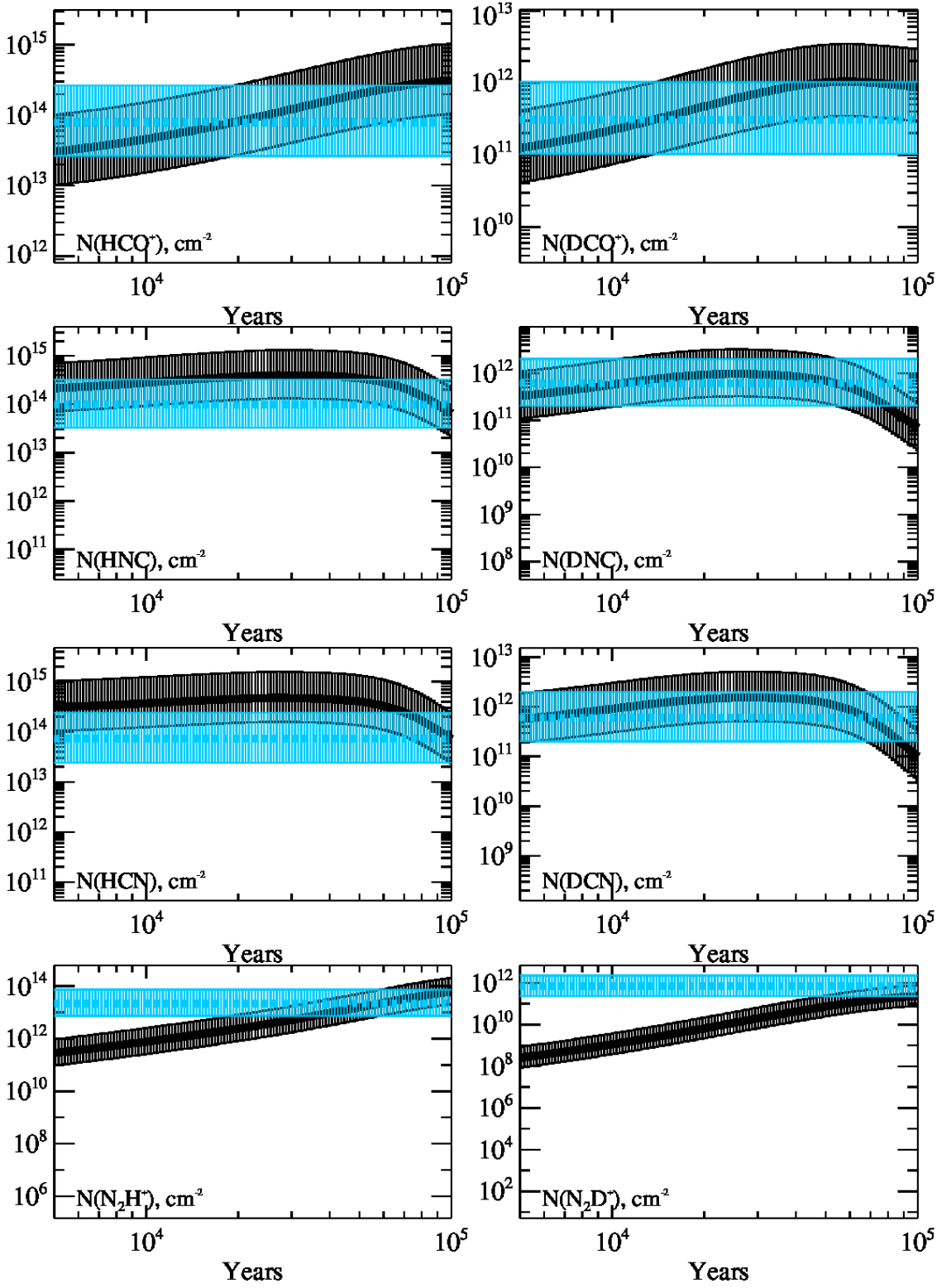


**Fig. A.1.** Observed and modeled column densities in  $\text{cm}^{-2}$  in the IRDC stage. The observed values are shown in blue, the modeled values in black. The error bars are indicated by the vertical marks. Molecules are labeled in the plots.

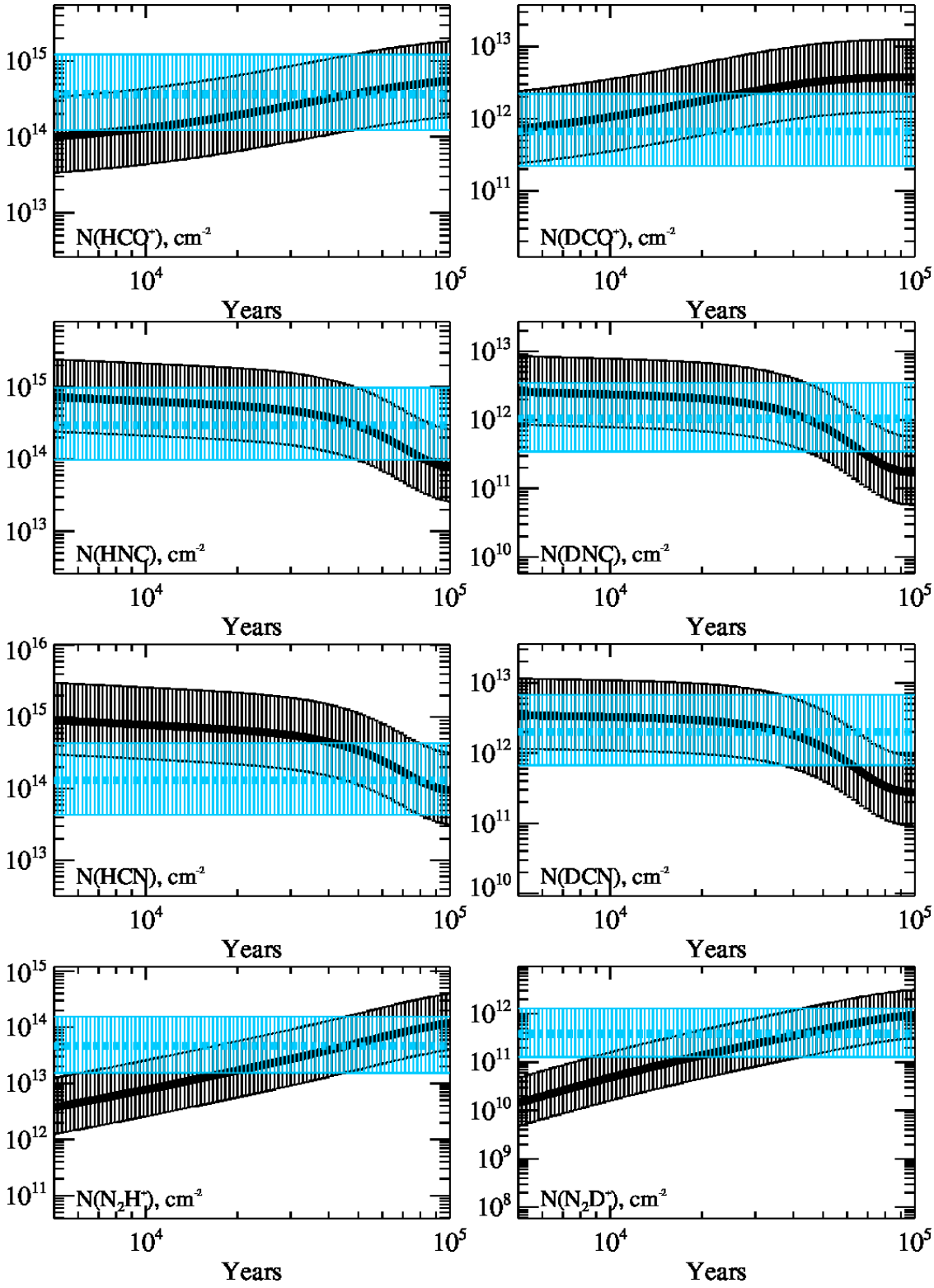


**Fig. A.2.** Observed and modeled column densities in  $\text{cm}^{-2}$  in the HMPO stage. The observed values are shown in blue, the modeled values in black. The error bars are indicated by the vertical marks. Molecules are labeled in the plots.

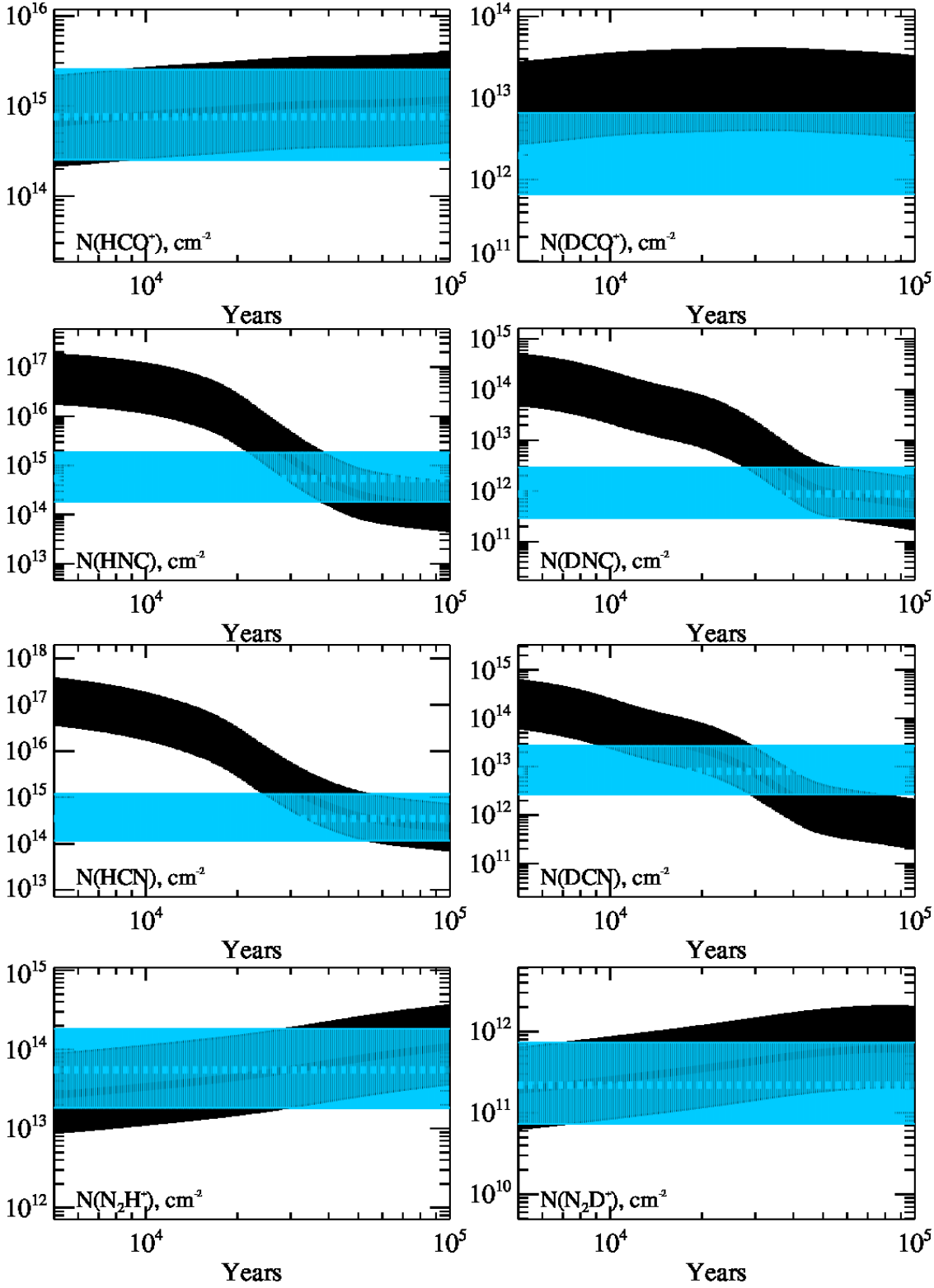


**Fig. A.3.** Observed and modeled column densities in  $\text{cm}^{-2}$  in the HMC stage. The observed values are shown in blue, the modeled values in black. The error bars are indicated by the vertical marks. Molecules are labeled in the plots.

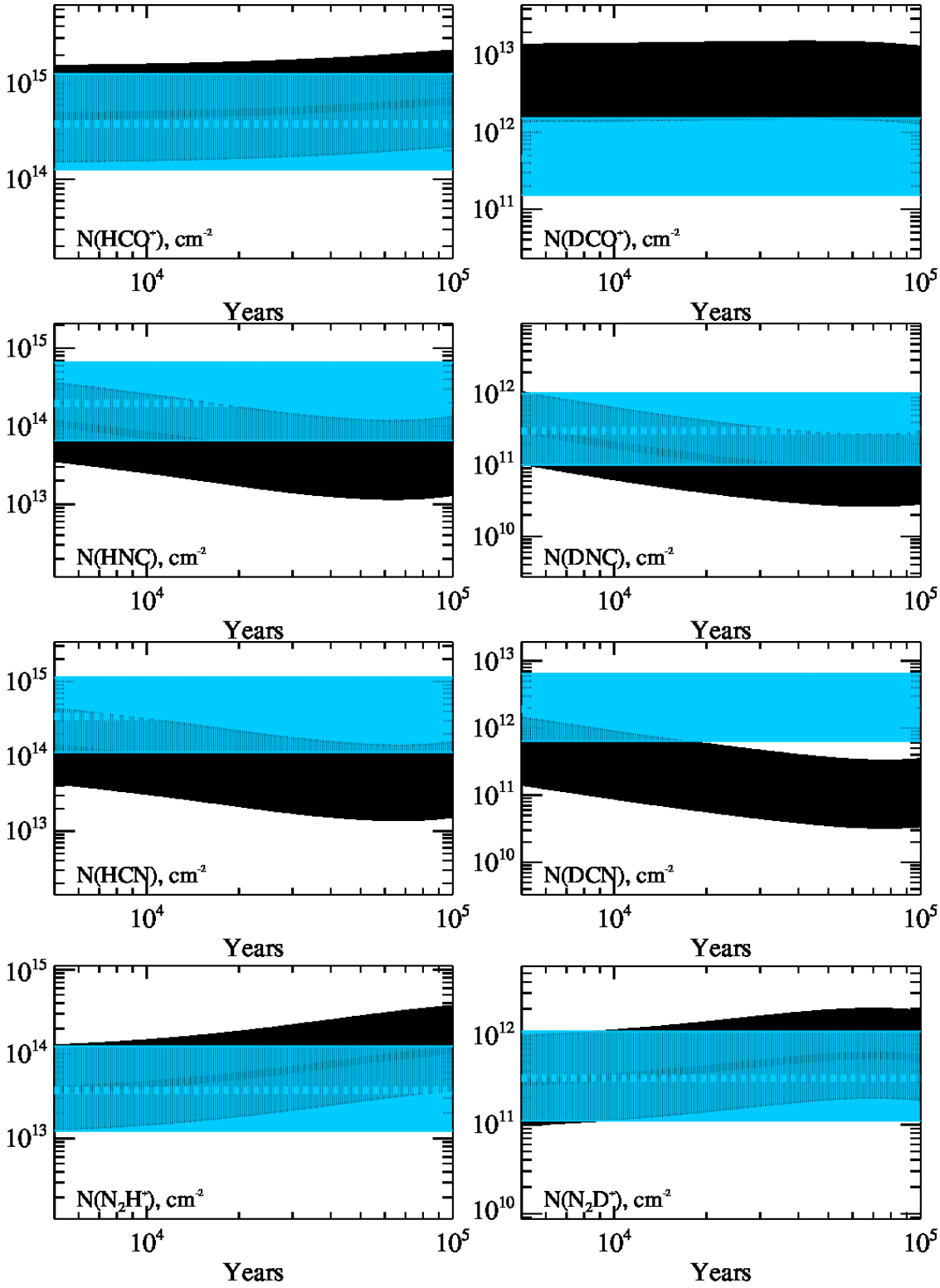


**Fig. A.4.** Observed and modeled column densities in  $\text{cm}^{-2}$  in the UCHII stage. The observed values are shown in blue, the modeled values in black. The error bars are indicated by the vertical marks. Molecules are labeled in the plots.